REPORT DOCUMENTATION PAGE

Form Approved
OMB No. 0704-0188

1. REPORT DATE *(DD-MM-YYYY)* 09 January 2017	2. REPORT TYPE Conference Paper with Briefing Charts	3. DATES COVERED *(From - To)* 01 December 2016 – 11 January 2017

4. TITLE AND SUBTITLE	5a. CONTRACT NUMBER
A Study of Acoustic Forcing on Gas-Centered Swirl-Coaxial Reacting Flows (Conference Paper with Briefing Charts)	
	5b. GRANT NUMBER
	5c. PROGRAM ELEMENT NUMBER
6. AUTHOR(S) Mario Roa, John W. Bennewitz, S. Alex Schumaker, Douglas G. Talley	5d. PROJECT NUMBER
	5e. TASK NUMBER
	5f. WORK UNIT NUMBER Q0YA

7. PERFORMING ORGANIZATION NAME(S) AND ADDRESS(ES) AND ADDRESS(ES) Air Force Research Laboratory (AFMC) AFRL/RQRC 10 E. Saturn Blvd. Edwards AFB, CA 93524-7680	8. PERFORMING ORGANIZATION REPORT NO.

9. SPONSORING / MONITORING AGENCY NAME(S) AND ADDRESS(ES) Air Force Research Laboratory (AFMC) AFRL/RQR 5 Pollux Drive Edwards AFB, CA 93524-7048	10. SPONSOR/MONITOR'S ACRONYM(S)
	11. SPONSOR/MONITOR'S REPORT NUMBER(S) **AFRL-RQ-ED-TP-2016-401**

12. DISTRIBUTION / AVAILABILITY STATEMENT

Approved for Public Release; Distribution Unlimited. PA Clearance Number: 16597 Clearance Date: 12/14/2016 The U.S. Government is joint author of the work and has the right to use, modify, reproduce, release, perform, display, or disclose the work.

13. SUPPLEMENTARY NOTES

For presentation at AIAA SciTech Meeting; Grapevine, Texas, USA; January 09 - 11, 2016
Prepared in collaboration with Sierra Lobo , Inc., UCLA; Conference Paper with Briefing Charts

14. ABSTRACT

The reacting flow from a single gas-centered, swirl-coaxial injector was studied in an optically accessible, high-pressure chamber, with and without high-frequency acoustic perturbations. The gas-centered, swirl-coaxial injector employed liquid rocket engine relevant propellants of gaseous oxygen and RP-2. The reacting flow field behavior at an operating chamber pressure of 3.2 MPa and varying momentum flux ratios were investigated. High-speed shadowgraph images along with OH* and CH* chemiluminescence images were taken to capture the liquid fuel film, droplets, and flame response under acoustic excitation. For the acoustic forcing studies, low amplitude transverse standing waves typically below 5% of the chamber pressure were generated to simulate transverse combustion instabilities. Proper orthogonal decomposition and dynamic mode decomposition were performed on the high-speed shadowgraph and chemiluminescence images to detect the flame response to acoustic forcing, to which in-plane flapping motion was observed for acoustic forcing and rotating soot clouds were a large structures associated with the reacting flow field.

15. SUBJECT TERMS

DMD = Dynamic Mode Decomposition; GCSC = Gas-Centered Swirl-Coaxial Injector; J = Momentum Flux Ratio; PN = Pressure Node; POD = Proper Orthogonal Decomposition

16. SECURITY CLASSIFICATION OF:			17. LIMITATION OF ABSTRACT	18. NUMBER OF PAGES	19a. NAME OF RESPONSIBLE PERSON S. Schumaker
a. REPORT **Unclassified**	b. ABSTRACT **Unclassified**	c. THIS PAGE **Unclassified**	SAR	44	19b. TELEPHONE NO *(include area code)* N/A

Standard Form 298 (Rev. 8-98)
Prescribed by ANSI Std. 239.18

A Study of Acoustic Forcing on Gas-Centered Swirl-Coaxial Reacting Flows

Mario Roa[1]
Sierra Lobo, Inc., Air Force Research Laboratory, Building 8451, Edwards AFB, CA, 93524

John W. Bennewitz[2]
UCLA, Air Force Research Laboratory, Building 8451, Edwards AFB, CA, 93524

Stephen Alexander Schumaker[3] and Douglas G. Talley[4]
Air Force Research Laboratory, Building 8451, Edwards AFB, CA, 93524

The reacting flow from a single gas-centered, swirl-coaxial injector was studied in an optically accessible, high-pressure chamber, with and without high-frequency acoustic perturbations. The gas-centered, swirl-coaxial injector employed liquid rocket engine relevant propellants of gaseous oxygen and RP-2. The reacting flow field behavior at an operating chamber pressure of 3.2 MPa and varying momentum flux ratios were investigated. High-speed shadowgraph images along with OH* and CH* chemiluminescence images were taken to capture the liquid fuel film, droplets, and flame response under acoustic excitation. For the acoustic forcing studies, low amplitude transverse standing waves typically below 5% of the chamber pressure were generated to simulate transverse combustion instabilities. Proper orthogonal decomposition and dynamic mode decomposition were performed on the high-speed shadowgraph and chemiluminescence images to detect the flame response to acoustic forcing, to which in-plane flapping motion was observed for acoustic forcing and rotating soot clouds were a large structures associated with the reacting flow field.

Nomenclature

DMD	=	Dynamic Mode Decomposition
GCSC	=	Gas-Centered Swirl-Coaxial Injector
J	=	Momentum Flux Ratio
PN	=	Pressure Node
POD	=	Proper Orthogonal Decomposition

I. Introduction

   Gas-centered swirl-coaxial injectors (GCSC) have seen an increase in interest over the past decade for rocket engine applications[1-4]. These injectors combine features of the coaxial air-blast and pressure swirl atomizers. Similar to coaxial air blast atomizers, a shear layer is formed between the gaseous and liquid propellants. For these injectors, the liquid propellant is injected tangentially through the outer annulus, imparting a swirl onto the liquid similar to the pressure swirl atomizers. The resulting shear and tangential forces are responsible for atomizing the liquid propellant. This injector is ideally suited for oxygen-rich staged combustion cycles and has been used successfully in the Russian RD-180[5] rocket engines. Although, great operational success has been achieved with these injectors, there is very little

---

[1] Research Scientist, Sierra Lobo, Inc. 10 E. Saturn Blvd, Building 8451, Edwards, CA 935324, Member

[2] Postdoctoral Research Scholar, UCLA., 10 E. Saturn Blvd, Building 8451, Edwards, CA 935324, Senior Member

[3] Research Engineer, AFRL/RQRC., 10 E. Saturn Blvd, Building 8451, Edwards, CA 935324, Senior Member

[4] Lead, Combustion Dynamic Group, AFRL/RQRC., 10 E. Saturn Blvd, Building 8451, Edwards, CA 935324, Associate Fellow

understanding regarding the full modes of operation these injectors experience at rocket relevant conditions and their susceptibility to combustion instabilities.

Most of the related studies performed using GCSC injectors have been focused on the atomization process of the liquid fuel sheet, hydrodynamic instabilities, and spray characteristics. Researchers at the Air Force Research Laboratory (AFRL)[6-8] have developed physics-based scaling laws for GCSC injector design through extensive cold flow experimental studies with a parametric variation of physical dimensions such as cup recess length (L_c shown in Figure 1). It has been shown that the liquid sheet length prior to break-up scales strongly with the momentum flux ratio (J) of the two propellants. Lightfoot $et\ al.$[6-8] showed that the liquid sheet/film break up length reaches an asymptomatic value for a critical J value, hence any operating J value greater than the critical $will$ result in the same film break up length. Experimental studies by Kim $et\ al.$[9] on the spray patterns for a GCSC injector performed at high pressures also identified J as the controlling parameter for the break up length. Schumaker $et.al.$[2] and Jeon $et\ al.$[10] studied the effect of the recess cup length L_c for GCSC injectors. They independently showed experimentally that L_c has very little effect on the film break-up length once a critical operating J value is reached. Eberhart $et\ al.$[11] investigated the the spray cone angle as a function of chamber pressure, observing that the cone angle from the swirling liquid sheet decreased with increasing chamber pressure.

As the bulk of the prior research has been focused on characterizing the spray pattern and design methodologies for GCSC injectors under cold flow conditions, there is very little understanding of how these injectors operate under reacting conditions. A numerical study by Muss $et\ al.$[12] demonstrated phenomenological differences between cold flow and hot-fire spray patterns, particularly droplet size. Pomeroy $et\ al.$[13] and Morgan $et\ al.$[14] studied the response of GCSC injectors to transverse instabilities, but no effort to characterize the flame in steady-state conditions was attempted as the combustion chamber produced a self-excited combustion instability.

This paper encompasses an experimental effort to describe the steady-state combustion behavior and the combustion response of a single GCSC injector under acoustic forcing conditions using high-speed imaging techniques. Varying momentum flux ratios were investigated for a single geometry GCSC injector to characterize steady-state operation, whereas one test condition was subjected to high-frequency, low amplitude transverse acoustic oscillations in a pressure node (PN) configuration for the forcing study. All experimental efforts were done at a high chamber pressure of 3.2 MPa, where simultaneous high-speed shadowgraph and OH*/CH* chemiluminescence images were taken to capture the flame behavior.

II. Experimental Setup

The GCSC injector was tested in the Combustion Stability Lab (EC-4) at Edwards AFRL CA, using RP-2 and gaseous oxygen. A detailed review of the complete system can be found in the work of Wegener $et\ al.$[15]. The system has since been upgraded to accommodate liquid hydrocarbon propellants. This test facility also has fuel systems capable of flowing gaseous fuels such as CH_4 and H_2 and/or cryogenic oxygen or gaseous oxygen. The facility is equipped with a Pacific Instruments data acquisition system that is used for diagnostic and system monitoring measurements. The GCSC propellants were ignited using a hydrogen/air torch at the operating chamber pressure with a capsule of nano-particulate additives photo-ignited by a Xenon flashbulb acting as a pre-ignition source for the torch. A detailed description for the ignition system can be found in the work of Badakshan $et\ al.$[16]

The experiment was performed within a high pressure, optically accessible combustor. A CAD rendering of the windowed combustor is shown in Figure 2. This windowed combustor features a chamber within a chamber design, where the large outer windows are used to contain pressure and the small inner windows are used to contain the flame. The windowed combustor features two piezo-sirens positioned on either side of the injector that are capable of generating an acoustic standing wave to force the flame/injector flow. The combustor's two large windows are used for the various line-of-sight imaging techniques (e.g., shadowgraphy). The combustor also features off-axis windows for future laser diagnostics measurements like particle image velocimetry (PIV) and planar laser induced fluorescence (PLIF). The windowed chamber is pressurized using a continuous flowrate of nitrogen gas and is not affected by the combustion process, as the volume occupied by the flame is small relative to the volume of the pressurizing nitrogen gas. This helps sever the thermo-acoustic feedback loop, effectively isolating the flame from any potential chamber coupled combustion instabilities.

Three high-speed cameras, (Phantom v710, v1210, and v2512) were used for the simultaneous shadowgraph, OH*, and CH* chemiluminescence.. All three cameras were synchronized using an IRIG time signal, along with the system measurements from the Pacific Instruments data acquisition system. A schematic of the optical setup for the three high-speed imaging techniques is shown in Figure 3. For the shadowgraph system, a broadband collimated light travels through two dichroic mirrors. This collimated light first encounters a dichroic mirror coated to reflect 410 nm to 450 nm light, and transmit in the higher visible wavelengths, towards the Phantom v2512 for CH* chemiluminescence.

The CH* chemiluminescence 431 nm light is captured by a Lambert Instruments HiCATT intensifier with a Semrock filter (FF01-425/26). The reflective surface of this dichroic mirror rejected the blue light portion from the broadband collimated light away from the intensifier and hence there was no need to pre-color filter this light to avoid saturating the intensifier. The second dichroic mirror is coated to reflect the UV light for the OH* chemiluminescence and transmits visible light used for the shadowgraphy system. The OH* chemiluminescence was also imaged using a HiCATT intensifier with a Semrock filter (FF01-320/40). The shadowgraph camera was set to a gate of 7 µs, with the intensifiers gated at 110 ns for OH* and 500 ns for CH*. The cameras captured images at 1000 Hz for a one second of steady-state combustion. For the acoustically-forced conditions, the image capture rate of the shadowgraph and CH* systems was increased to 25 kHz for 0.2 seconds, while the OH* system was set to a lower frame rate to capture one second of the acoustically-forced flame.

As can be seen in Table 1, four test conditions were investigated with different J values of oxidizer-to-fuel momentum flux. For each test condition, the RP-2 flowrate was kept constant while the gaseous oxygen flow was varied to achieve different J values. The flowrates of RP-2 and gaseous oxygen were measured using a Siemens Coriolis mass flow meter (SITRANS FC) and Porter Thermal mass flow meter (Type 123), respectively. The windowed combustor was pressurized to 3.2 MPa using gaseous nitrogen prior to ignition. From these four conditions, Test 4 was selected to be acoustically forced. During these experiments, the piezo-sirens were operated 180° out-of-phase to form a standing wave pressure node (PN) condition in the vicinity of the reacting flow field, where a PN and corresponding velocity anti-node (VAN) was located at the injector location. Three differential pressure transducers (Kulite XCL-100) were mounted to one of the inner windows to measure the pressure amplitude, phase, and shape of the standing wave during testing. These inner windows were also coated with an oleophilic coating that spread RP droplets optical thin, thus not obscuring the view to the flame.

Table 1. Operating Conditions and Average Cone Angles

Test	$\dot{m}_{RP-2}(g/s)$	$\dot{m}_{ox}(g/s)$	Φ	J	P_c (MPa)	Left Side STD Θ	Right Side STD Θ
001	1.36	5	0.92	5.5	3.26	5.27	10.45
002	1.40	5.67	0.84	6.45	3.3	5.79	9.94
003	1.40	4.56	1.04	4.4	3.21	6.84	9.90
004	1.37	4.62	1	4.88	3.17	5.58	7.88

III.   Results

A.   Average Behavior

For each test condition, one second of steady-state flame operation was averaged using each optical method and can been seen in Figure 4. The vertical green line shown in this figure represents 10 mm of the flow field beginning at the nozzle exit plane. For the CH* averages, the view is partially blocked downstream by the differential pressure transducer used to characterize the standing wave for acoustic forcing studies. From both the CH* and OH* average images, it is observed that the flame is separated from the nozzle for each test condition. Great care must be taken in interpreting this behavior, since the average shadowgraph images show the flame is attached at the nozzle exit. By overlapping the CH* and shadowgraph average images, as shown in Figure 5, an apparent spatial offset exists between where the CH* is first observed and the flame at the injector exit present in the shadowgraph average. Related experiments done at AFRL show strong indications of burning in the cup recess. Those related experiments have shown decomposed fuel deposits on the injector face, significant heat flux into the injector and evolved injector face temperatures, which are all experimental findings indicating burning in this portion of the injector. Purdue University has also measured OH* and CH* directly in the injector. It is currently believed that the flame is anchored within the cup recess of the injector for these studies, and it is observed that combustion takes place in the near injector region and at times the chemiluminescence is obscured from view. It will be shown later from the instantaneous shadowgraph images that highly luminous pockets of reacting RP are observed to be attached to the nozzle exit, then are later obstructed from view by either a soot cloud or by the liquid RP sheet emanating from the nozzle.

From Figure 4, Tests 2 and 3 both show an asymmetric flame structure present in the average OH* and CH* images. This asymmetry is not fully understood since a consistent asymmetry is not present for the other two test conditions. In the X-ray radiography cold flow studies performed by Schumaker *et al.*[13], an asymmetry of the mass distribution in the swirling spray was observed at different operating conditions for a single injector. It is possible that

a similar mechanism is occurring during Tests 2 and 3, where greater concentrations of fuel are present at different spray locations, resulting in higher CH* and OH* concentrations at those locations.

There is also an asymmetry present in the cone angle formed by the spray. In Figure 6, the standard deviation of the shadowgraph images were used to measure the cone formed by the reacting flow field. The standard deviation images were chosen over the averages for the cone angle Ө measurement as there were more pronounced edge boundaries of the reacting flow field present in the standard deviation images. These cone angle measurements were performed by visual inspection and are presented in Table 1. As the cone angles significantly differ between the left and right spray edge boundaries for all test conditions, an unequal cone angle contributing to this asymmetry is observed. Further investigation will be necessary to address the physical mechanisms leading to this asymmetry.

B. Instantaneous Behavior

A time series of the instantaneous shadowgraph, CH*, and OH* images for Test 4 are shown in Figures 7, 8, and 9, respectively. In the shadowgraph and OH* images, a soot cloud can be viewed rotating about the gaseous oxygen core. The soot clouds corresponds to the dark regions in the flow field that obscure the view to the flame. As mentioned earlier, this soot cloud surrounds the oxygen core and blocks the view to the flame and its anchoring regions. Occasionally, highly luminous reacting pockets can been seen to attach to the injector exit in Figure 7. Given the CH* and OH* averages indicate the flame is separated from the nozzle but is visibly attached within the nozzle in the shadowgraph average and instantaneous images in Figure 7, it is vital that direct observation of the flame within the injector is needed to verify the flame's anchoring location.

The soot cloud near the injector droplet field obscuring the near field region of the flame is caused by the design of the injector. GCSC injectors are designed to have a fuel-rich outer layer that helps keep the injector face from overheating. In a multi-element configuration, this fuel flow across the injector is pushed downstream when fuel from neighboring elements meet in the interelement regimes. This creates a fuel-rich mixture that breaks down as it is heated, creating a soot cloud that can block light emission in the UV and visible spectrums.

Observation of the high-speed videos shows the soot cloud originates from the periphery of the swirling liquid sheet, which is consistent with a fuel-rich mixture breakdown being responsible for the soot formation. The soot cloud also rotates in the direction of the swirl and hence carries the angular momentum imparted by the swirl. The generated soot clouds convect at much slower velocity compared to the oxygen core and the flame. Unreacted fuel droplets are also observed to be shed from the periphery of the liquid sheet. Although droplets were observed in the flow field, the spatial resolution was not high enough to provide droplet statistics for these studies. The OH* chemiluminescence was also very diffusive compared to the other two viewing methods and it is not fully understood why this is the case at the moment. From the instantaneous CH* images, it was observed that the luminous zones were created in isolated pockets, indicating that the flame this not spatially continuous but instead reacts in isolated regions. These isolated pockets were observed to extend further downstream from the field of view and hence no flame length statistics were extracted for these studies.

C. Proper Orthogonal Decomposition

Proper orthogonal decomposition (POD) was select to study the large structures associated with the flame and rotating soot cloud present in the instantaneous images. Only the POD analysis for Test 4 will be discussed in greater detail as the results for the other test conditions yielded similar findings. The POD analysis decomposes a time series of images into spatially orthogonal structures, with each spatial mode having an energy and temporal component. A representation of the most dynamic flow features can be reconstructed by combining the most dominant POD modes[14]. This POD analysis was performed on the average image subtracted fluctuating component (i.e., instantaneous image minus the average image) for each optical method.

The energy associated with each mode from the shadowgraph, CH*, and OH* POD results are shown in Figure 10. From this analysis, there is no dominant mode present in the flow field, but instead the modal energies have a linear relationship. This indicates that reconstructing a representative flow field of the dynamic processes is only possible by combining hundreds of modes, as there are no truly dominant modes. This lack of dominant modes indicates that the rotating soot cloud is very chaotic and turbulent. Inspecting the certain spatial modes along with the fast Fourier transform (FFT) of the corresponding temporal mode, the rotation of the soot cloud about the oxygen core can be observed along with its physical spatial scales. This is given by the alternating red and blue pattern, which represents changes in light intensity caused by the soot cloud blocking the view to the flame. This pattern is independently detected with each optical viewing method, hence the soot cloud is a dominant flow field structure in these studies.

Multiple frequency peaks are present within the single spatial mode shown in Figure 11. These multiple frequency peaks indicate that the creation of the soot clouds and their rotation about the oxygen core is irregular. A similar observation can made by performing an FFT (shown in Figure 12) on the pixel intensity that is 15 inner injector diameters away from the nozzle exit. This location was chosen as it encompasses the average path taken by the soot clouds throughout the one second of high-speed images captured. From Figure 12, multiple frequencies are also present without a defined peak, similar to the POD temporal modes.

D. Acoustically Forced Results

For the acoustically forced studies, Test 4 was studied in greater detail. The injector was forced at six different chamber resonant frequencies, corresponding to PN excitation, spanning from 1920 Hz to 3430 Hz. For each of the six forcing frequencies, the standing wave pressure amplitude was set to 20.68 KPa (3 Psi). Using the definition of DMD decomposition, where

$$I(x,y,t) = Real(\sum_{j=1}^{N} A_j \exp(i2\pi f_j \Delta t) DM_j), \hspace{2cm} \text{Eq. 1}$$

$I(x,y,t)$ is the time series video, A_j is the amplitude or modal energy of component j, i is the imaginary number coefficient, f_j is the complex frequency of mode j, Δt is the time separation between each frame, and DM_j is the complex spatial mode j. In DMD, each spatial mode j has a unique complex frequency f. We can define the sensitivity of the reacting flow to the acoustic forcing by comparing the A_j relative to its neighboring spatial modes, as comparing A_j to its neighbors is similar to comparing frequency peaks from power density plots to its neighbors.

Figure 13 shows the A_j values for the unique frequencies of each DM_j, similar to a power density plot. The results for the shadowgraph high-speed video will be discussed further as the CH* DMD output yielded similar results. It should be noted that dynamic mode decomposition was not applied to the unforced conditions as temporal resolution for these experiments was not high enough as per the Nyquist criteria. For the forcing cases, however, the DMD analysis shows the strongest peaks relative to the neighboring spatial modes is strongest for 1920 Hz and 3060 Hz forcing. The shape of the spatial mode can be seen in Figure 14 for the forcing frequency 1920 Hz and 3060 Hz. For both frequencies, the acoustic perturbations impose the same shape to the flow, where the injector experiences in-plane flapping motion. The in-plane flapping is imposed onto the central gaseous oxygen flow, behaving almost as a single jet. The in-plane flapping motion is given by the yellow and blue bands directly across from each other right below the nozzle exit. The effect on the acoustic perturbations on the liquid film or droplets was not observed.

The in-plane flapping motion can be observed by viewing the temporal evolution of mode j at the forcing frequency f_j detected by the DMD analysis. The temporal evolution of the spatial mode throughout time can be created by using Eq.1. By selecting the mode j of interest and marching Δt in time, the time evolution of a specific mode can be created. The temporal evolution of mode j associated with 1920 Hz can be seen in Figure 15. The spatial mode was cropped to focus on the behavior near the nozzle exit. The red and blue pattern alternate along a given side of the gaseous oxygen core. This alternating pattern is due to the in-plane flapping motion of the gaseous oxygen core. The physical interpretation of this red and blue pattern is changes in light intensity associated with the flame along the oxygen core swaying side to side.

Summary and Conclusions

Although the results presented here cover a small amount of the vast physical processes associated with GCSC injectors, there are several findings from this experimental study. Among the findings are the following:

- Flame appears to be separated from the nozzle exit as shown in the CH* and OH* chemiluminescence average image, but attached in the shadowgraph images

- Depending on the operating J condition, the flame is asymmetric

- Cone angle formed by the flow is also asymmetric

- Soot cloud is created at the outer periphery of the swirling, liquid sheet

- Soot cloud is non-periodic in nature and rotates about the oxygen core, blocking the flame's chemiluminescence

- Soot cloud convects slowly compared to the oxygen core and the flame

- From the POD analysis, the lack of high energy modes and presence of the multiple strong frequency peaks indicate that the soot cloud is highly stochastic in its creation and rotation about the oxygen core

- The gaseous oxygen core behaves similar to a single jet under acoustic forcing

- From the DMD analysis, the GCSC injector has shown a sensitivity to the frequency of the external acoustic field

It is suspected that the sensitivity of the injector to the acoustic forcing can be due to injector geometry, but will have to be investigated further. Future work will be identifying if the momentum flux ratio dominants the dynamics of the reacting flow as it does for the cold flow studies. Given the limited range of *J* values tested here, no conclusions can presently be drawn regarding the influence the momentum flux ratio has on the reacting flow field. Sensitivity and its subsequent behavior to acoustic excitation under a pressure anti-node configuration will also be investigated. Combined, these future studies will extend the current knowledge of GCSC injectors.

ACKNOWLEDGMENTS

References

[1]Canino, J., Heister, S., Sankara, V., and Zakharov, S., "Unsteady Response of Recessed-Post Coaxial Injectors", *41st AIAA/ASME/SAE/ASEE Joint Propulsion Conference and Exhibit, AIAA 2005*-4297, Tucson*, AZ, 2005*

[2]Schumaker, S. A., Danczyk, S, A. and Lightfoot, M .D .A., " Effect of Swirl on Gas-Centered Swirl-Coaxial Injectors", *47st AIAA/ASME/SAE/ASEE Joint Propulsion Conference and Exhibit, AIAA 2011-4297,* San Diego, 2011

[3]Lightfoot, M. D. A., Danczyk, S.A., and Talley, D.G. "Atomization in Gas-Centered Swirl-Coaxial Injectors,*" 19th ILASS Americas,* Toronto, Canada, 2006

[4]Schumaker, S.A., Danczyk, S.A., and Lightfoot, M.D.A. "Effect of Cup Length on Film Profiles in gas-Centered Swirl-Coaxial Injectors,*" 48th AIAA Aerospace Sciences Meeting,* 2010-368, Orlando, Fl, 2010.

[5]Dranovsky, M.L., "Combustion Instabilities in Liquid Rocket Engines: Testing and Development Practices in Russia,*" Progress in Astronautics and Aeronautics*, Vol. 221, 2007.

[6]Lightfoot, M. D. A,. Danczyk, S. A., and Talley, D. G., "A method to predict atomization performance in gas-centered swirl-coaxial injectors," Technical Paper No. AFRL-PR-ED-TP-2007-125

[7] Lightfoot, M. D. A,. Danczyk, S. A., and Talley, D. G., "Atomization rate of gas-centered swirl-coaxial injectors," Technical Paper No. AFRL-RZ-ED-TP-2008-074

[8]M. D. A. Lightfoot, S. A. Danczyk, and D. G. Talley, "Scaling of gas-centered swirl-coaxial injectors," Technical Report No. ADA502809

[9]Kim. J. G., Han, Y. M., Choi, H. S., and Yoon, Y., "Study on spray patterns of gas-centered swirl coaxial (GCSC) injectors in high pressure conditions" Aerospace Science and Technology, 27 (2013)

[10] Jeon, J., Hong, M., Han, Y. M., and Lee, S. Y., "Experimental Study on Spray Characteristics of Gas-Centered Swirl Coaxial Injectors," Journal of Fluids Engineering, (133) 2011

[11] Eberhart, C. J., Lineberry, D. M., and Moser, M. D., "Effects of Variable Chamber Pressure on Swirl Coaxial Injection: A Cold Flow Study," *46th AIAA/ASME/SAE/ASEE Joint Propulsion Conference and Exhibit*, AIAA 2010-368 Nashville, TN, July 2010.

[12] Muss, J. A., Johnson, C. W., Cheng., G. C., and Cohn, R. K., "Numerical Cold Flow and Combustion Characterization of Swirl Coaxial Injectors," *41th Aerospace Sciences Meeting*, Reno, NV, Jan 2003

[13] Pomeroy, B, R,. Sisco, J, C., Eckstein, J, R,. and Anderson, W. E., " Characterization of Gas-Centered Swirl-Coaxial Injector Stability in a Subscale Mutli-Element Combustor," *44th AIAA/ASME/SAE/ASEE Joint Propulsion Conference & Exhibit*, AIAA 2008-5249, Hartford, CT, 2008

[14] Morgan, C., Shipley, K. J., and Anderson W. E., "Comparative Evaluation Between Experimental and Simulation for a Transverse Instability," Journal of Propulsion and Power, (31) No 6 2015

[15] Wegener, J, L., Leyva, I. A., Forliti, D. J., and Talley, D. G., "Development of a Facility for Combustion Stability Experiments at Supercritical Pressure," *52nd AIAA Aerospace Sciences Meeting*, 2014-0317, National Harbor, MD, 2014

[16]Badakshan, A., Danczyk, S., Forliti, D., Levya, I., and Talley, D., "Nano-ignition Torch applied to cryogenic H2/O2 Coaxial Jet," *54th AIAA Aerospace Sciences Meeting*, 2016-0184, San Diego, Ca, 2016

[17] Schumaker, S. A., Kastengren, A. L., Lightfoot, M. D., Danczyk S. A., and Powell, C. F., "A study of Gas-Centered Swirl Coaxial Injectors Using X-ray Radiography," *12th Triennial International Conference on Liquid Atomization and Spray Systems,* Heidelberg, Germany, Sept 2-6, 2012

[18] Roy, S., Hua, J. C., Barnhill, W., Hunaratne, and Gord, J. R., " Deconvolution of reacting-flow dynamics using proper orthogonal and dynamic mode decompositions," Phys. Rev. E 91, 013001
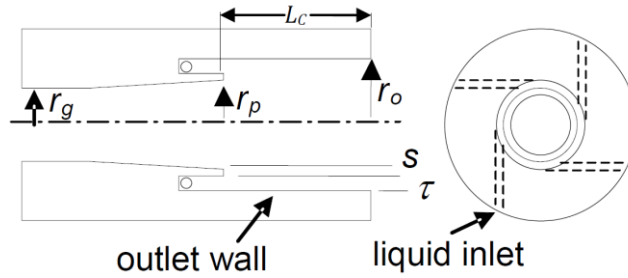
Figure 1. A schematic of a gas-centered swirl-coaxial injector, where r_g represents the initial gas radius, L_c the injector cup length, r_p the gas post radius at the end of the sheltering lip, r_o the outlet radius, S the step height and τ the initial film thickness.
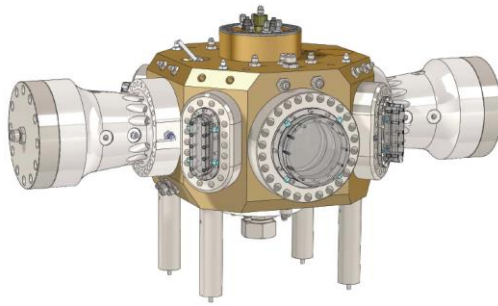
Figure 2. A CAD rending of the high pressure, windowed combustor.
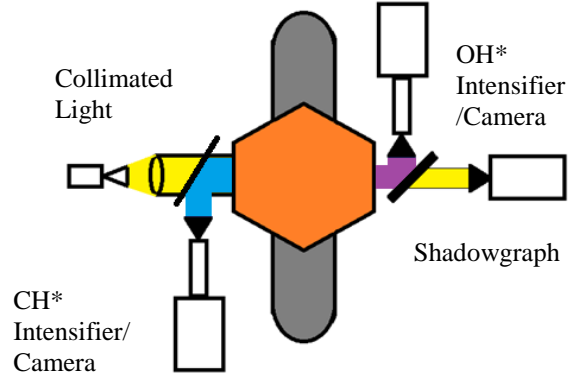
Figure 3. A schematic of the optical setup. A collimated light passed through two dichroic mirrors used for CH* and OH* chemiluminescence. The blue represents the 431nm CH* chemiluminescence, the purple 308nm OH* chemiluminescence, and the yellow the broadband collimated light for used for shadowgraph.

a)

b)

c)
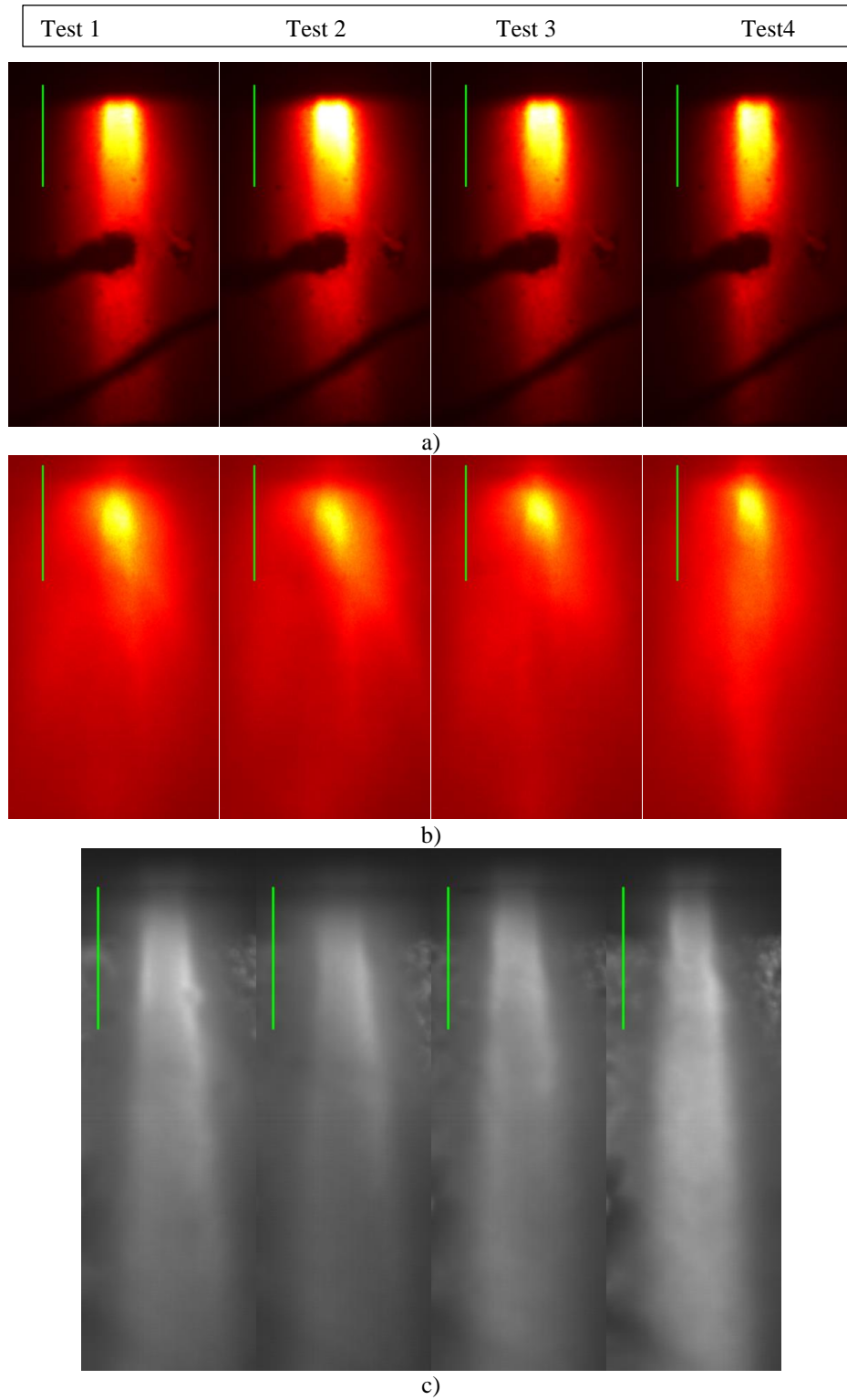
Figure 4 - (a) False color CH* average, (b) False color OH*average and (c) Shadowgraph average. The vertical green line is located at the nozzle exit plane and is 10 mm in length. Note that images are not at the same scale. From left to right, the averages are from Test 1, 2, 3, and 4, respectively.
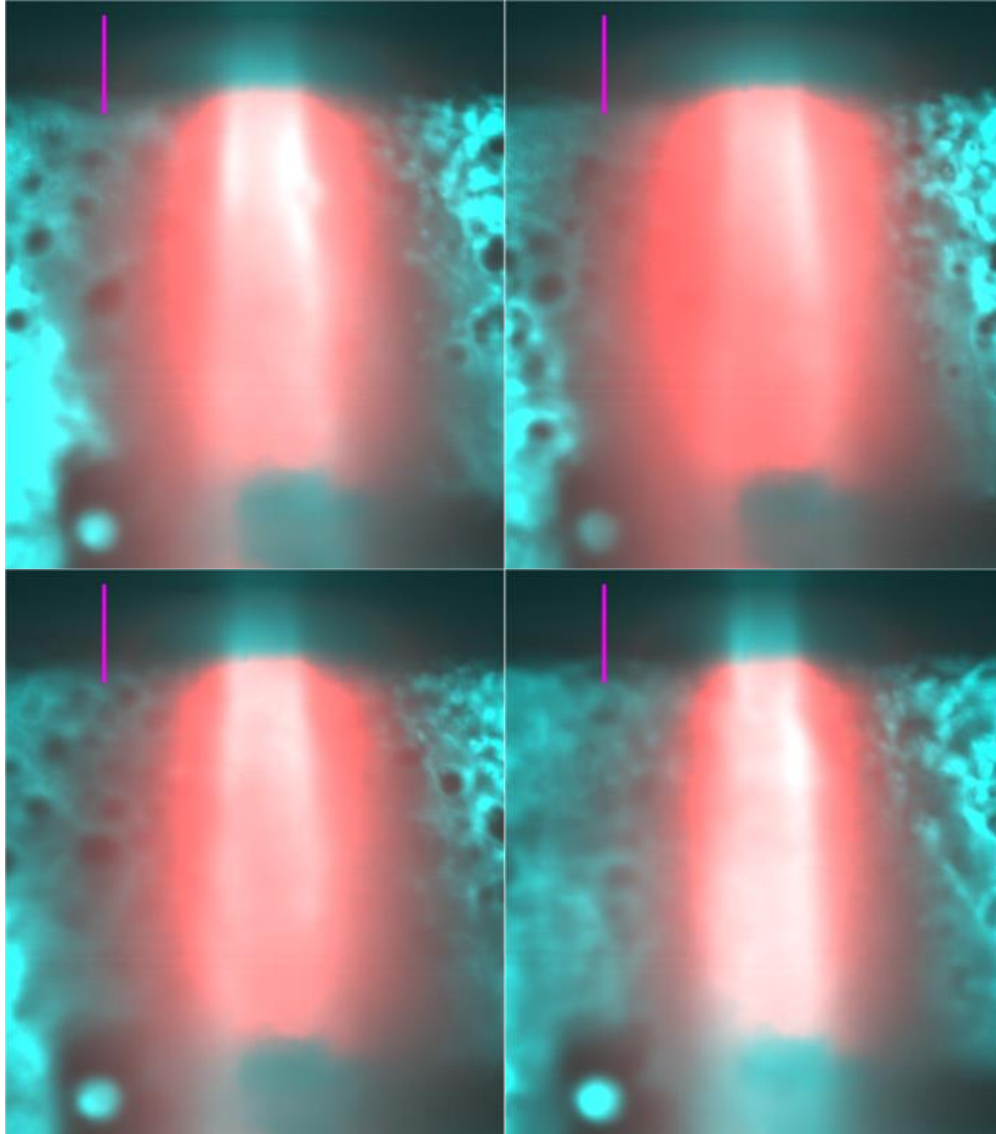
Figure 5 – Wavelet fused image of shadowgraph and CH* averages. The red represents the CH*, while the blue background represents the shadowgraph. The purple vertical line is 3 inner core diameters from the nozzle exit. Top row from left to right is Test 1, 2 and bottom row, left to right is Test 3 and4, respectively.

American Institute of Aeronautics and Astronautics
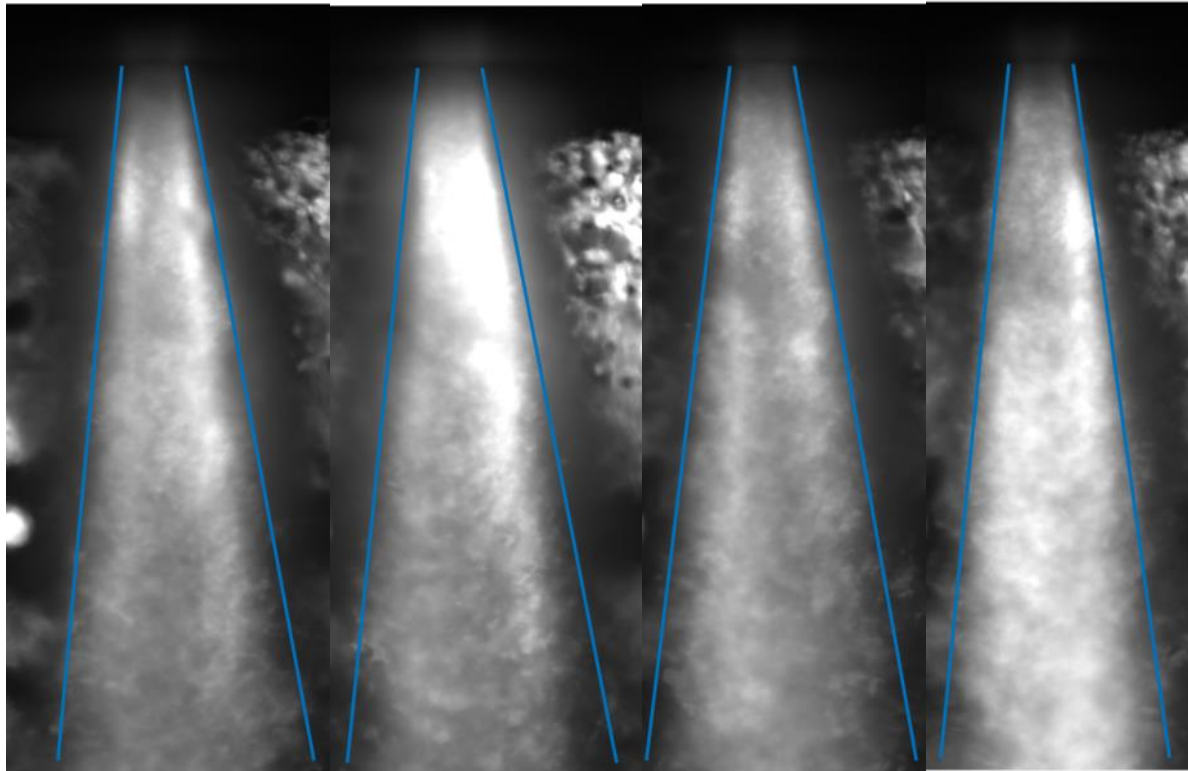
Figure 6 – Standard Deviation pixel intensity from the shadowgraph images. The blue represent the spread of the cone. From left to right is Test 1, 2, 3, 4, respectively.
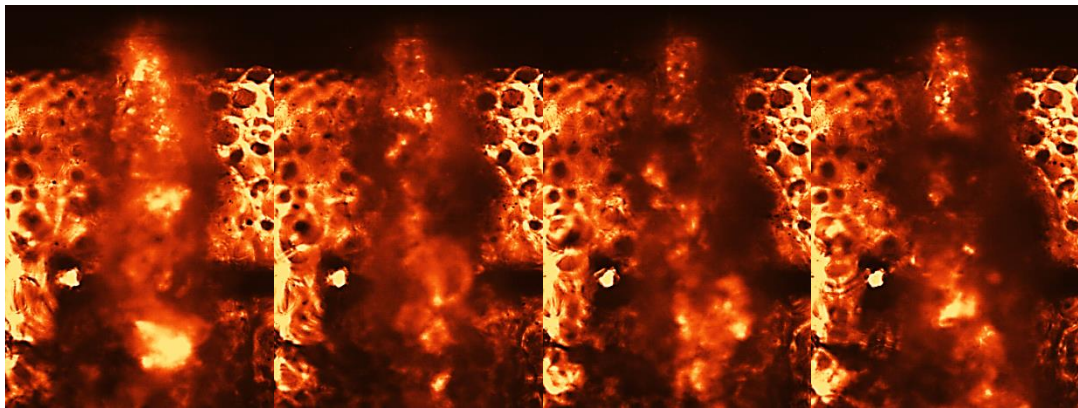
Figure 7 – Time series of an instantaneous shadowgraph images. A dark soot cloud can be seen obstructing the view to the center core.

American Institute of Aeronautics and Astronautics
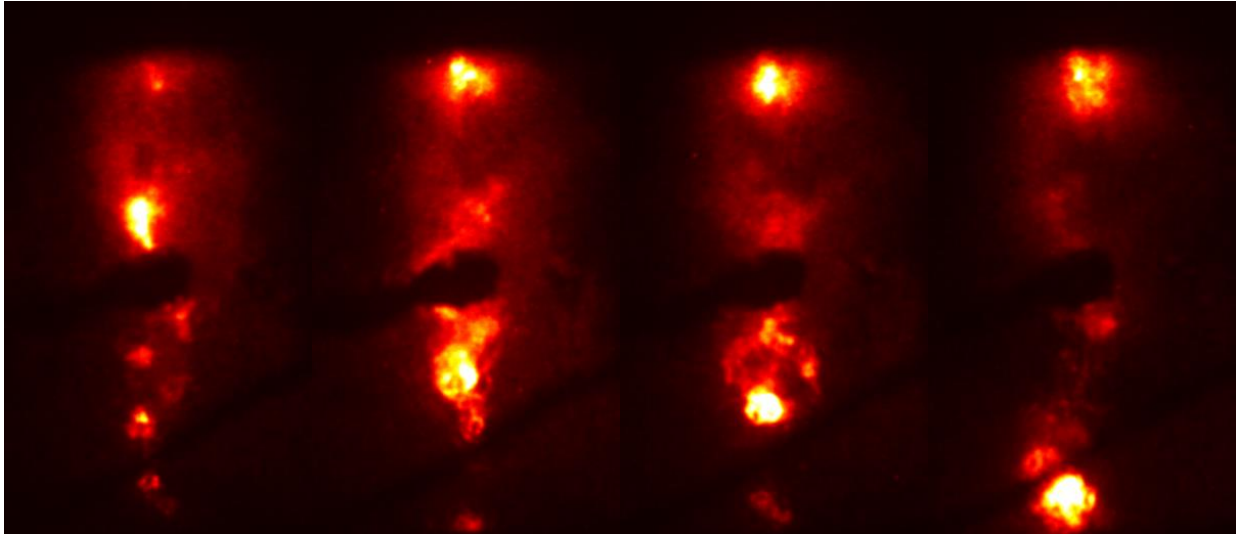
Figure 8 – Time series of an instantaneous CH* images. The flame is longer than the field of view. The differential pressure transducer is blocking part of the view.
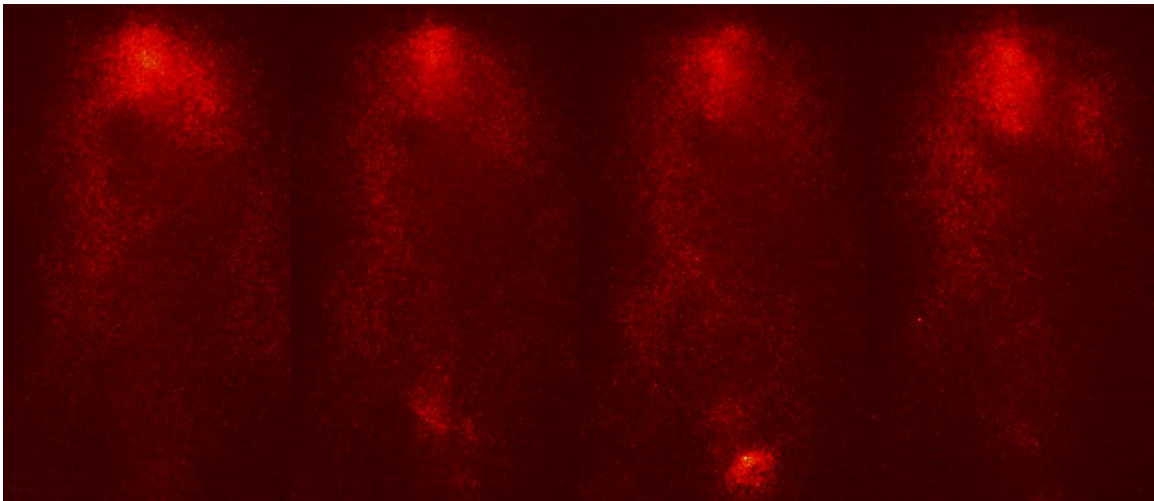
Figure 9 – Time series of an instantaneous OH* images. The flame is longer than the field of view and the soot cloud obstructs the same regions as the shadowgraph.

American Institute of Aeronautics and Astronautics
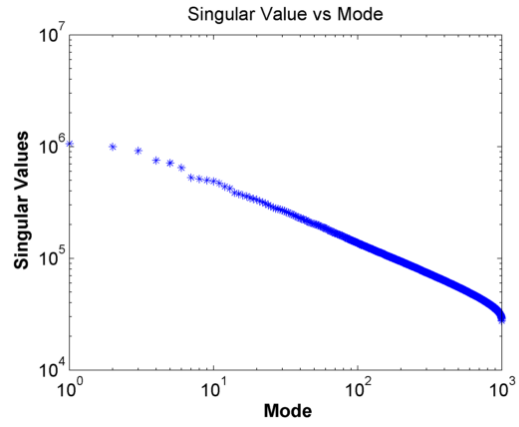
a)
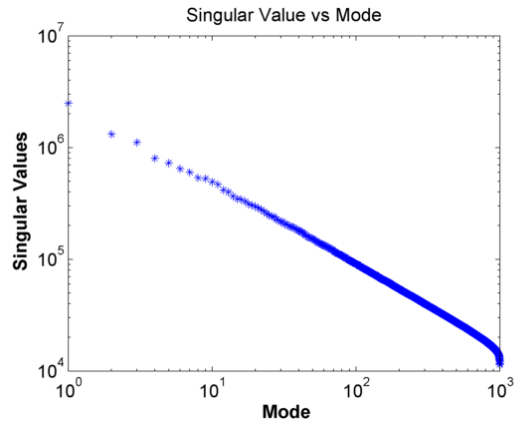
b)
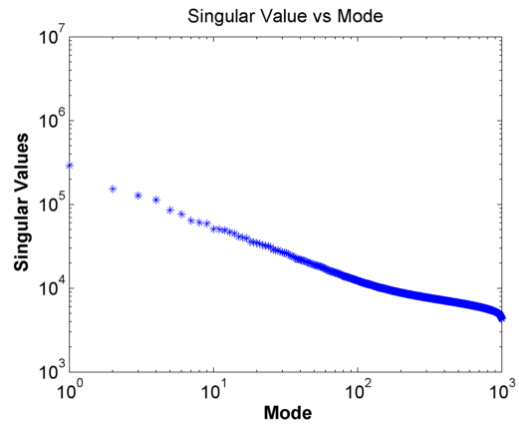
c)

Figure 10 – POD Energy values associated with each POD spatial mode. a) Shadowgraph, b) CH*, and c) OH*.

American Institute of   Aeronautics and Astronautics
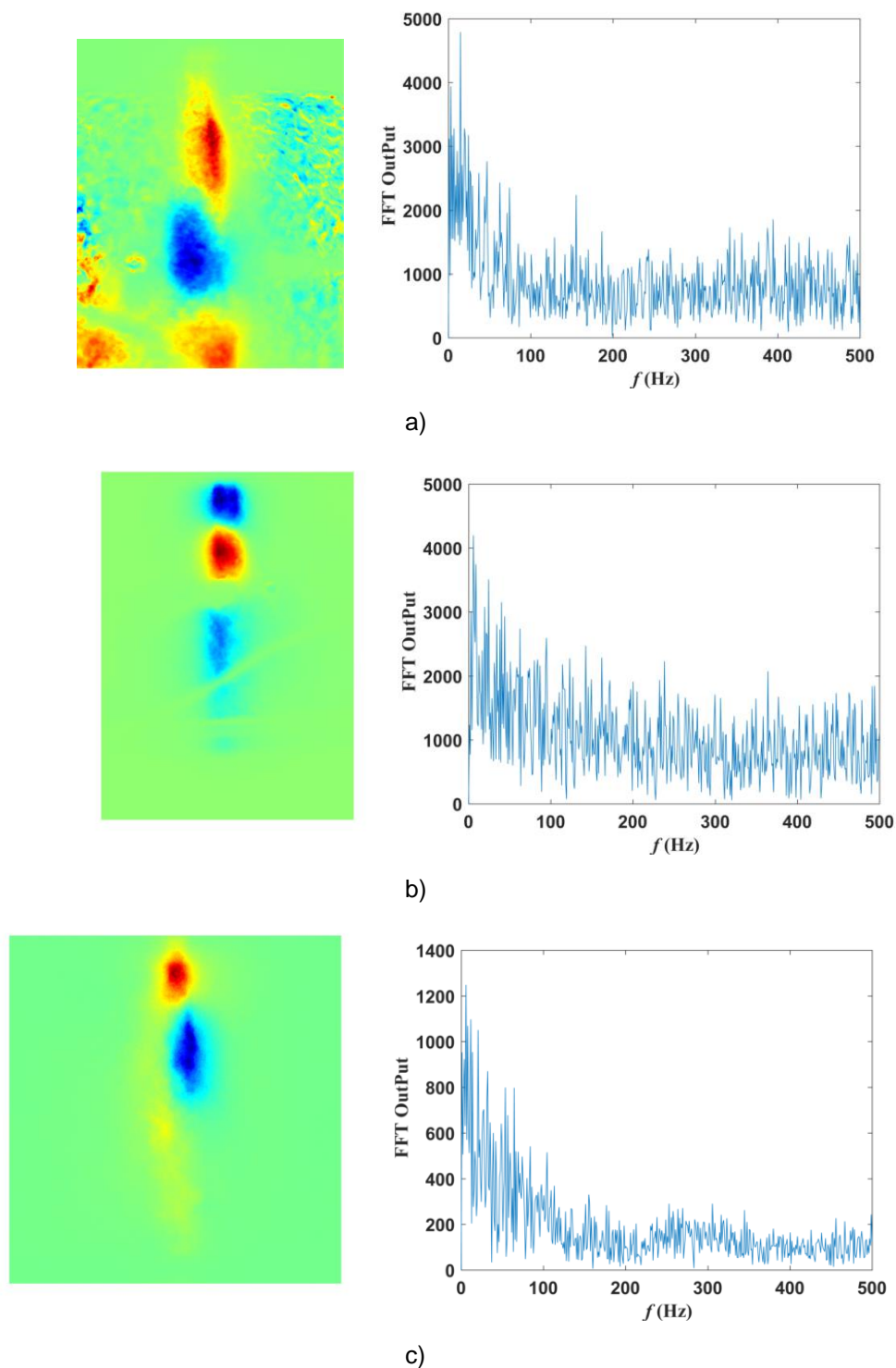
Figure 11 – A POD Spatial mode and FFT of the corresponding temporal mode. A) Shadowgraph, B) CH*, and C) OH*. The alternating pattern is due to the soot cloud blocking the flame's chemiluminescence.

American Institute of   Aeronautics and Astronautics
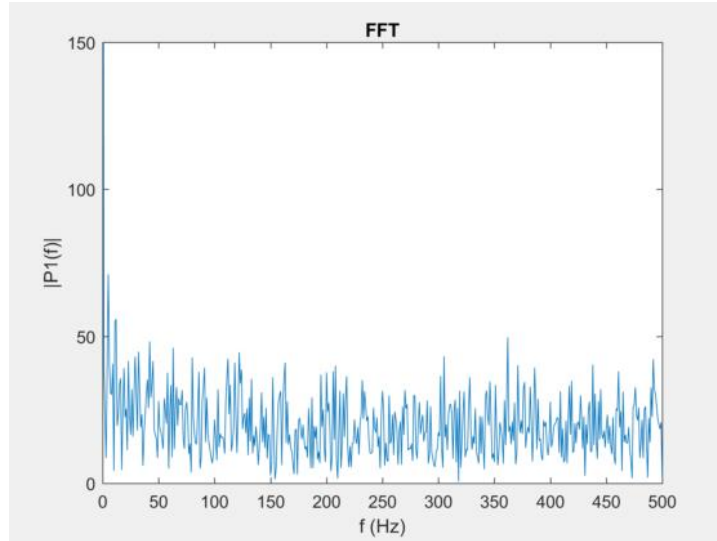
Figure 12 – A FFT of the pixel intensity from the shadowgraph images taken 15 oxygen diameters away from the nozzle exit.

a)

b)

c)

d)

e)

f)
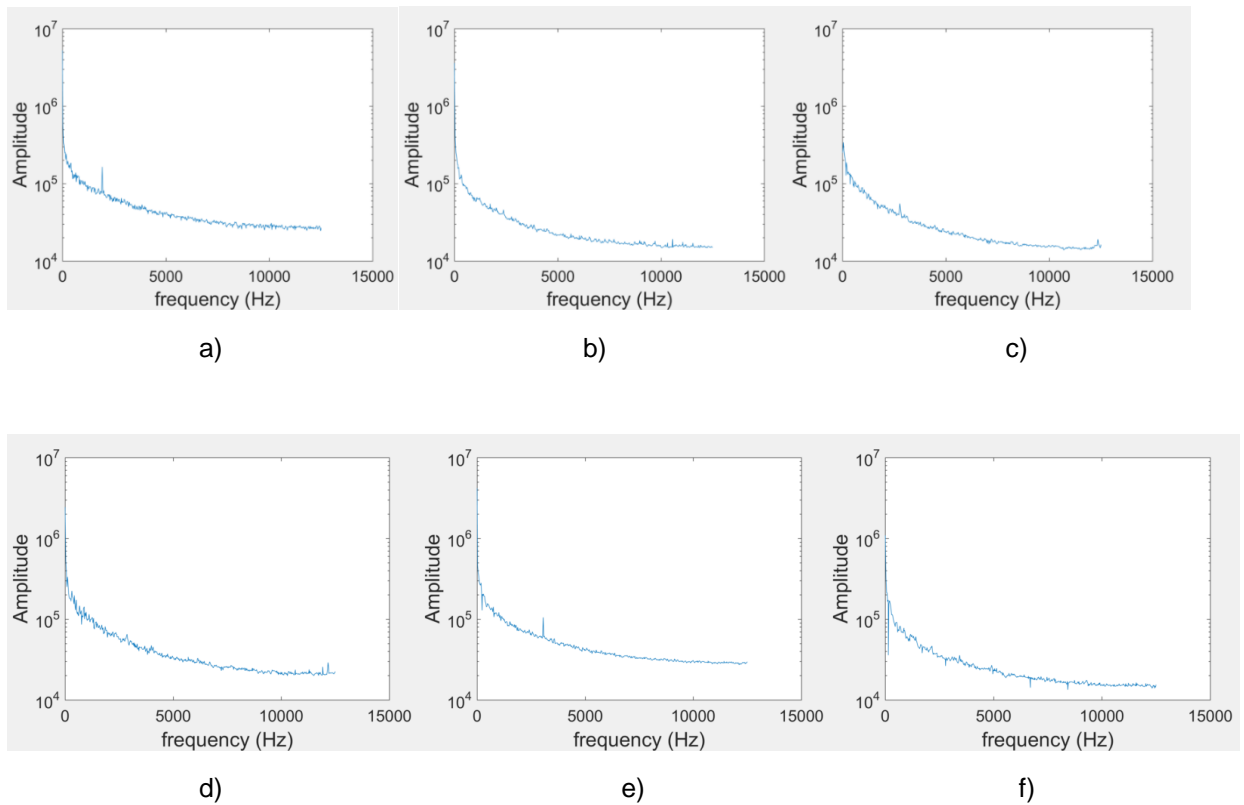
Figure 13 – The DMD amplitude A vs the frequency. a) is 1930 Hz, b) 2380 Hz, c) 2780 Hz, d) 2852 Hz, e) 3060 Hz, and f) 3430 Hz.
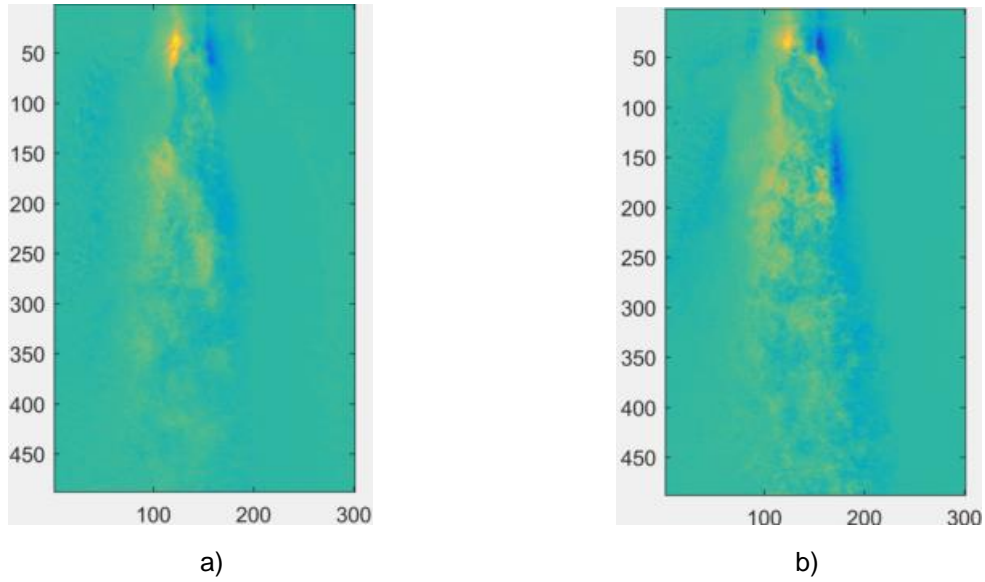
Figure 14 – The DMD spatial mode extracted from the high-speed shadowgraphy for a) 1920 Hz, and b) 3060 Hz. The alternating band is indicative of a in-plane flapping.
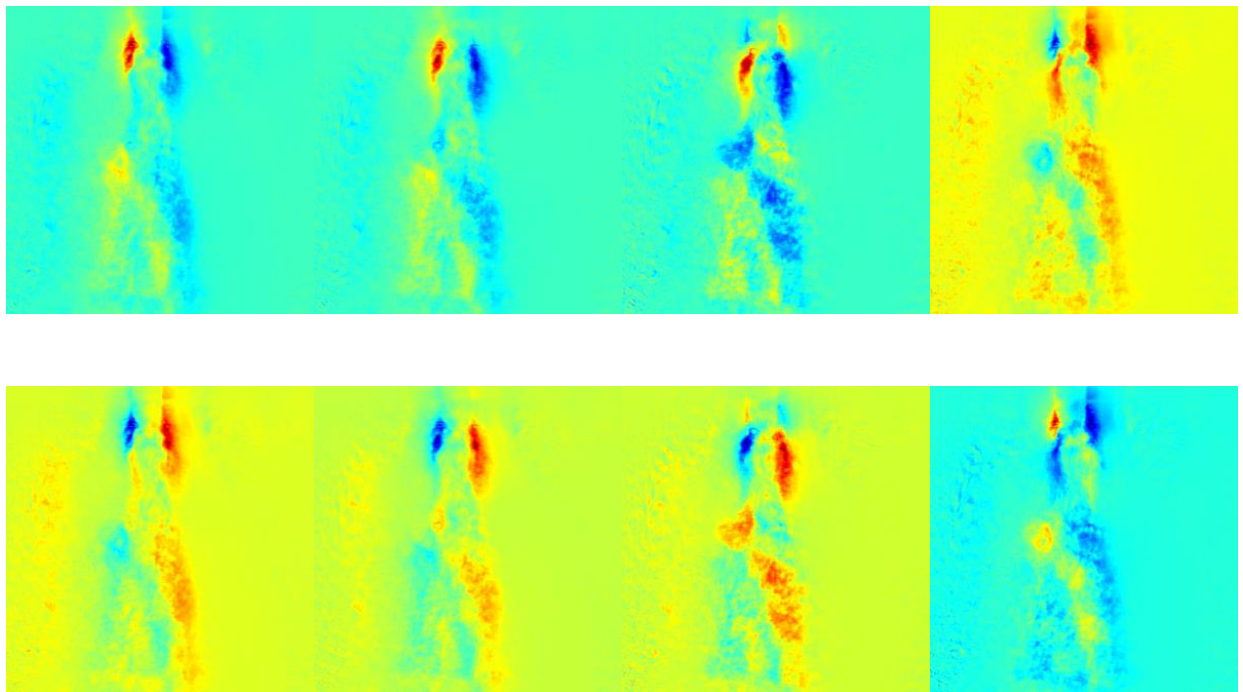
Figure 15 – The DMD spatial mode temporal evolution extracted from the high-speed shadowgraphy of the 1920 Hz acoustic perturbations. An in-plane flapping motion is indicative by the changing red and blue pattern.

A Study of Acoustic Forcing on Gas-Centered Swirl-Coaxial Reacting Flows

55th AIAA SciTech Meeting
Grapevine, Tx, January 2017

Mario Roa, Sierra Lobo, Inc.
John William Bennewitz, UCLA
S. Alexander Schumaker, AFRL
Doug Talley, AFRL

AF relevant considerations

- **Achieving modern thermodynamic efficiencies requires achieving increasingly higher chamber pressures, sometimes exceeding the critical pressure of the reactants**
  - e.g., liquid rockets, future gas turbines

- **When the combustion systems are for propulsion, limited tankage dictates that on-board propellants be stored in condensed form**
  - e.g., kerosene, liquid oxygen in rockets

- **Combustion systems can no longer be designed to meet modern requirements without considering system dynamics**

- **Combustion dynamics always includes acoustic waves, which in enclosed systems can sometimes reach detrimental amplitudes**
  - e.g., combustion instabilities

Objectives

- **Study a single geometry sub-scale gas centered, swirl coaxial injector (GCSC) in a high pressure environment using ambient RP-2 and gaseous Oxygen**

- **Study the reacting flow field using three optical methods simultaneously.**
  - **Shadowgraph**
  - **CH* Chemiluminescence**
  - **OH* Chemiluminescence**

- **Study the reacting flow field for various momentum flux ratios *J*.**

- **Perform a sensitivity study of the injector geometry to acoustic perturbations.**

Approach

Acoustic
waves

Thermoacoustic
Instability
Mechanism

Open the
loop for
better
control

Hydrodynamic
response

Unsteady
Heat release
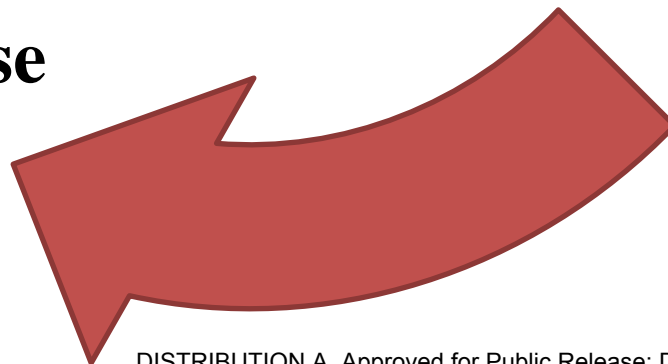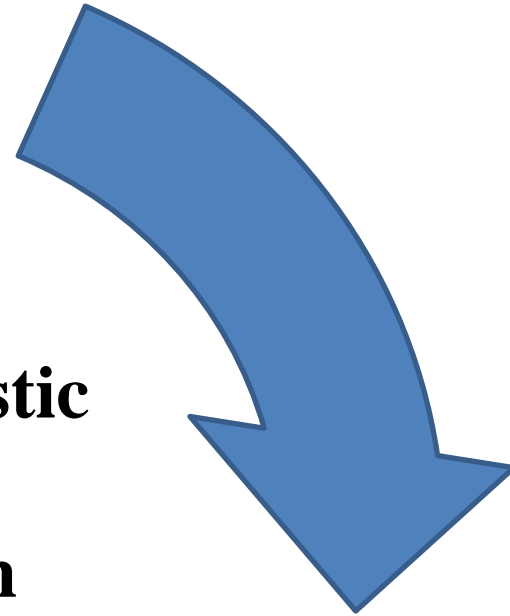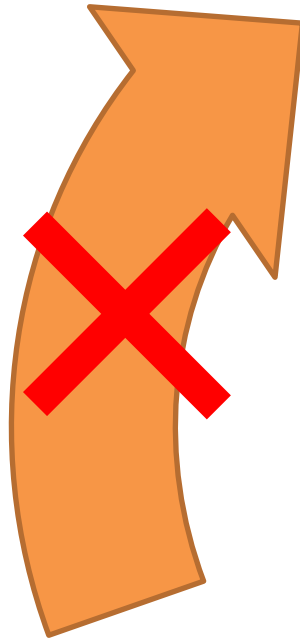
Gas Centered Swirl Coaxial Injector

Features

- **Oxygen rich gas is injected through the center of the injector.**

- **Liquid fuel is injector tangentially from the center flow.**

- **A swirling film is created and shrouds the inner gaseous flow**

- **The film is atomized due to shear and tangential forces**

L_C

r_g r_p r_o

s

τ

outlet wall   liquid inlet
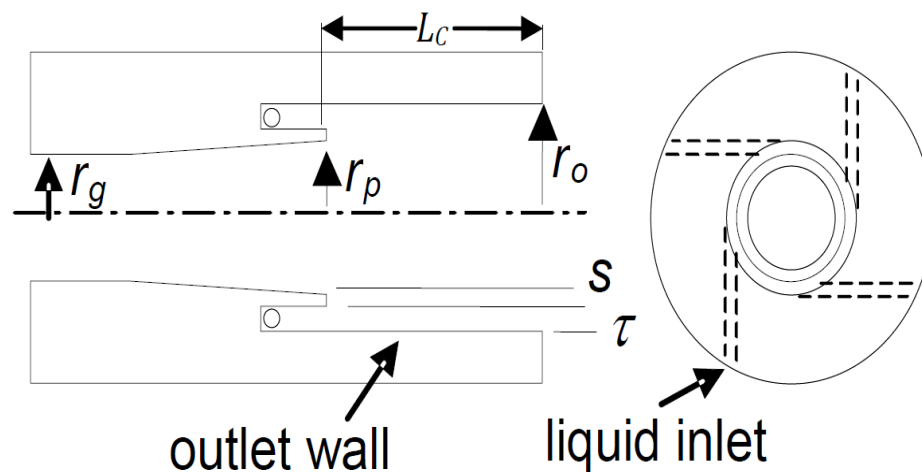
Experimental Facility
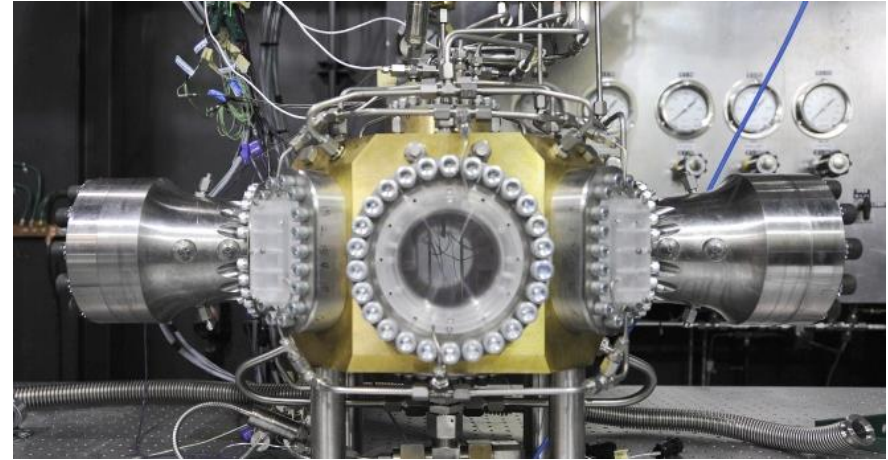
Features

- Frequency and amplitude independent of combustion – accurate control of frequency and amp.
- Pressurization independent of combustion – accurate control of pressure.
  - Subcritical and supercritical pressures
- Precise cryocooler – accurate control of temperature to within ±1 K.
- Chamber-within-a-chamber
  - Outer chamber contains pressure – pressure containing elements remain cool
  - Inner chamber contains acoustics and combustion only – allows finer adjustment of inner elements
- High amplitude piezosirens specially designed for high pressure
- On-axis windows for shadowgraph, Schlieren, chemiluminescence, OH* emission
- Off-axis windows for PIV/PLIF
- Fully developed turbulent injector flows – well known boundary conditions
- High-speed pressure transducers

Rayleigh Index fields

Summary of Forcing Conditions

- **Pressure node (PN) and pressure antinode (PAN) at the injector location**

PN
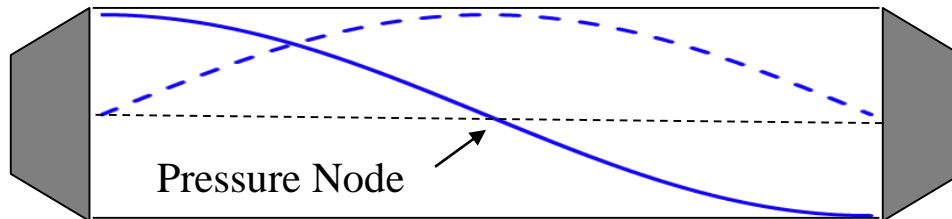
Imposes transverse velocity oscillation

Pressure Node

Velocity Node

PAN
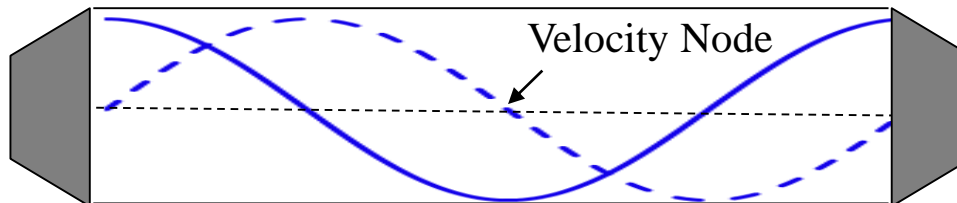
Imposes unsteady backpressure

- **Forcing frequency ~ 3000 Hz**

- **Pressure fluctuation amplitudes (peak-to-peak) range up to approximately 9 psi (6 psi reacting)**

Operating Conditions

- **Study four _J_ operating conditions at 3.2 MPa (460 Psi)**

- **_J_ ~ 4.4 to 6.5**
- **Fuel Velocity – 6.5 m/s**
  Oxygen Velocity – 58.7 m/s

- **Kept fuel massflow the constant and varied oxygen to achieve the desired _J_ value**

- **Use the optical set up of shadowgrpahy, CH* and OH* chemiluminescence.**

- **Acoustically force the reacting flow to at 6 resonant pressure node conditions from 1920 Hz to 3430 Hz. The pressure node was kept constant.**

- **Collected 1000 frames at 1000 fps for average behavior and then 5000 frames at 25kHz for the acoustic studies.**
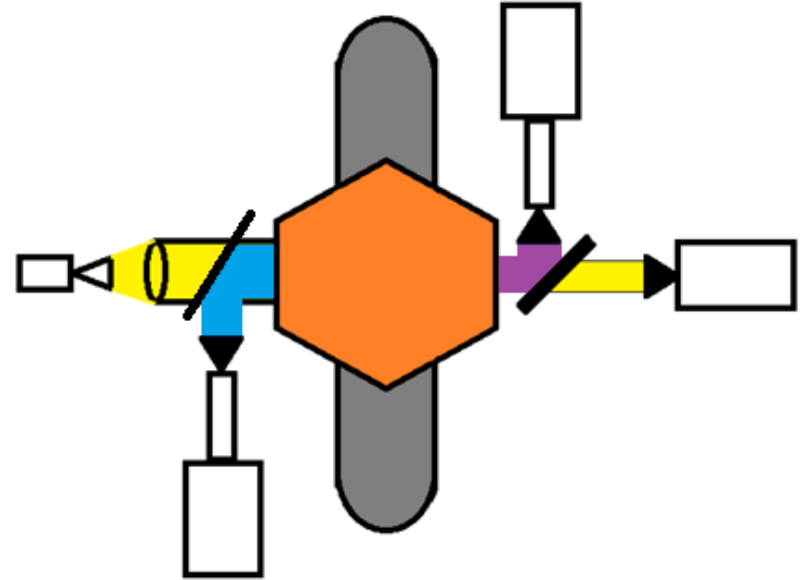
Unforced Results (J = 4.8)
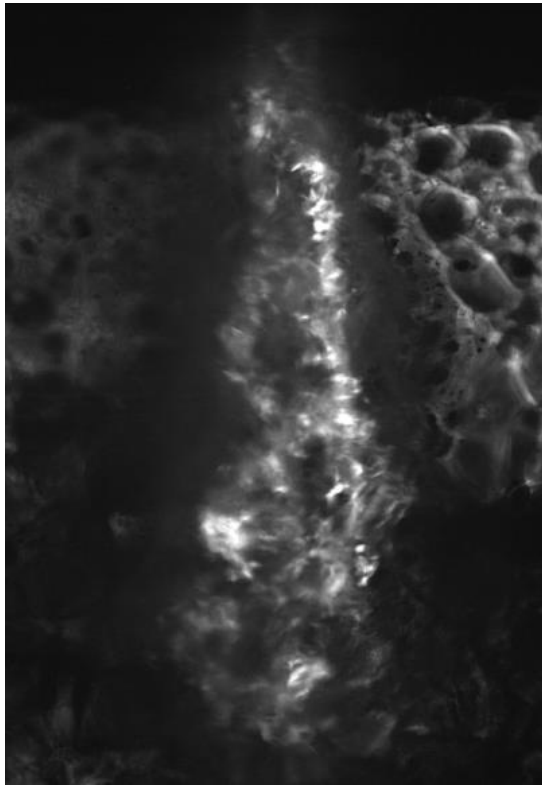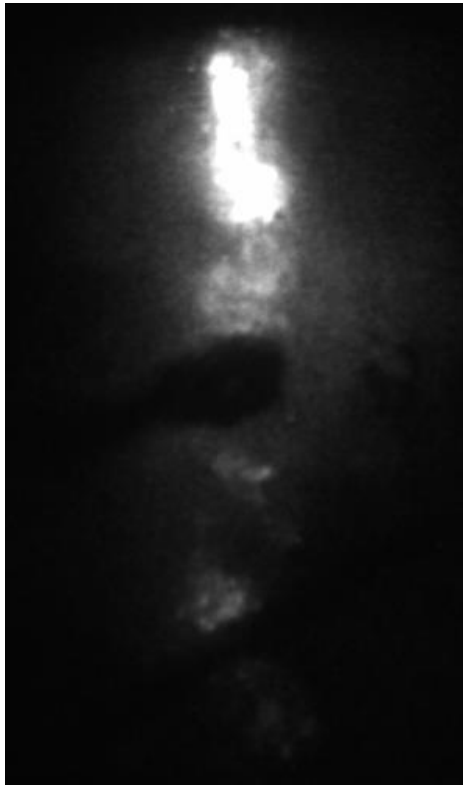
Shadowgraph   CH*   OH*
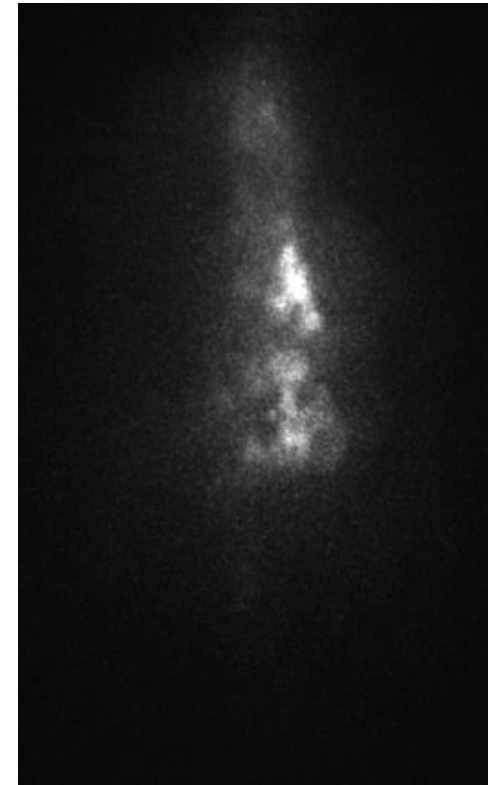
- **Soot clouds are created at the periphery of the swirling film.**

Unforced Results Shadowgraph Average
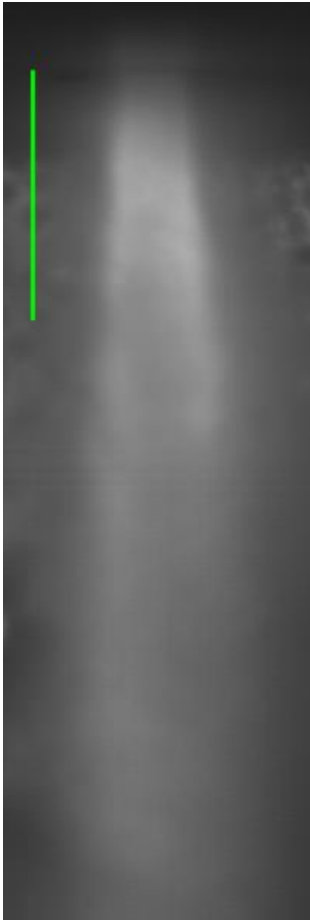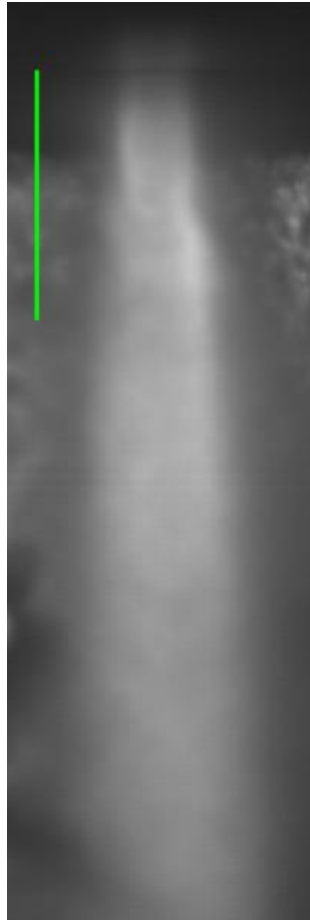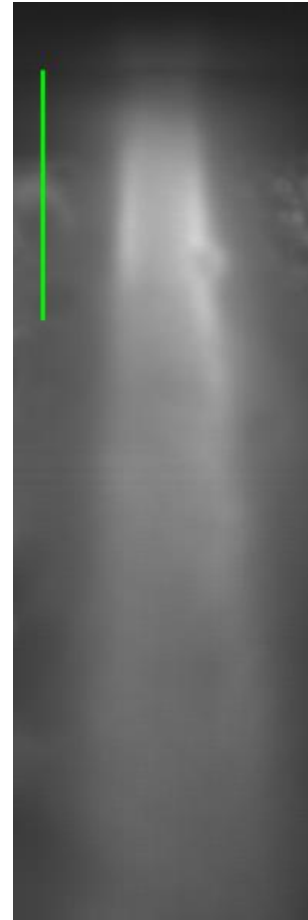
J = 4.4   J = 4.8   J = 5.5   J = 6.5

- **The flame is attached to the nozzle exit.**
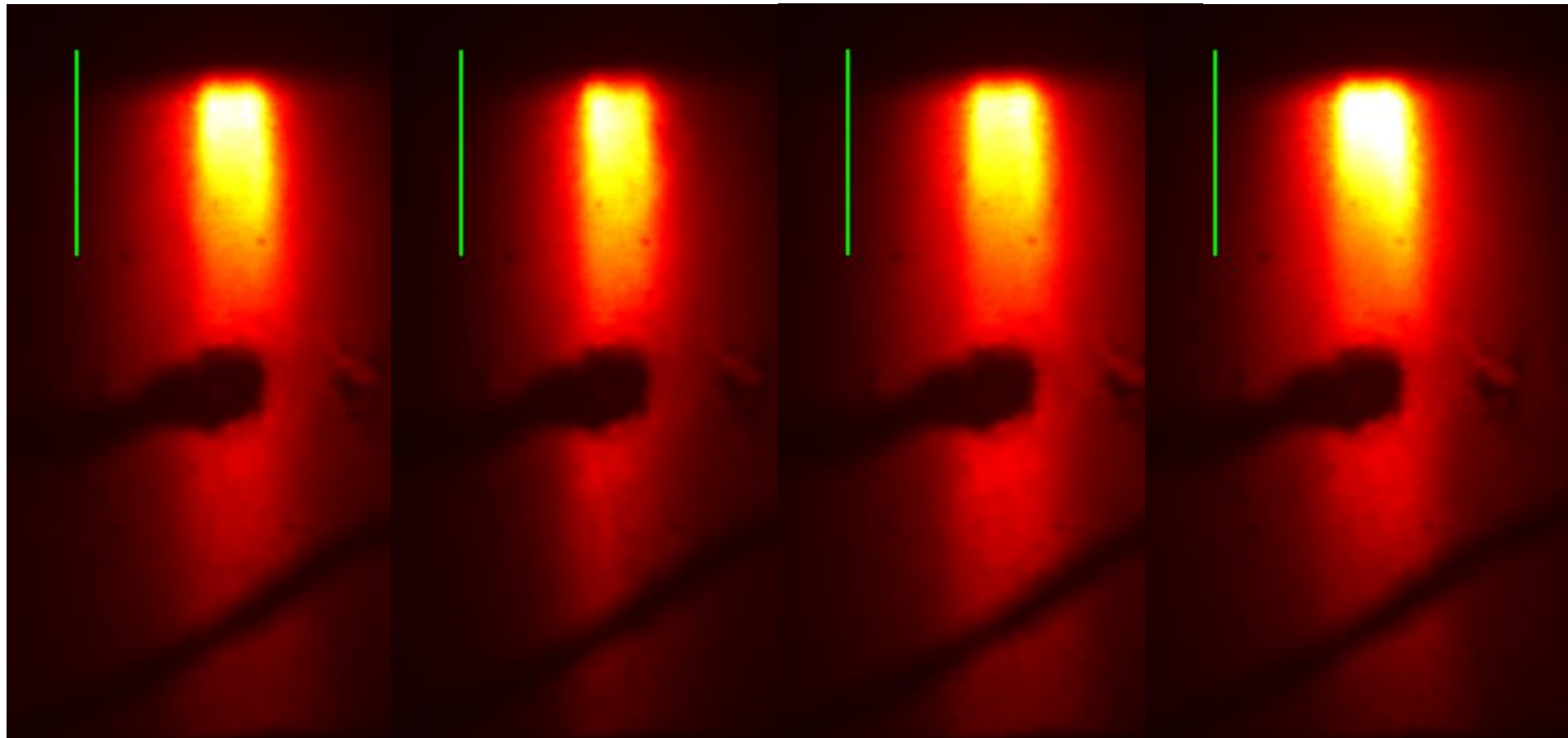
J = 4.4 J = 4.8 J = 5.5 J = 6.5

- **A flame appears to be separated from the nozzle.**

J = 4.4   J = 4.8   J = 5.5   J = 6.5

- **From the CH* average (in red) it is separated from the nozzle 3 inner jet diameters away from the nozzle.**

Unforced Results OH* Average
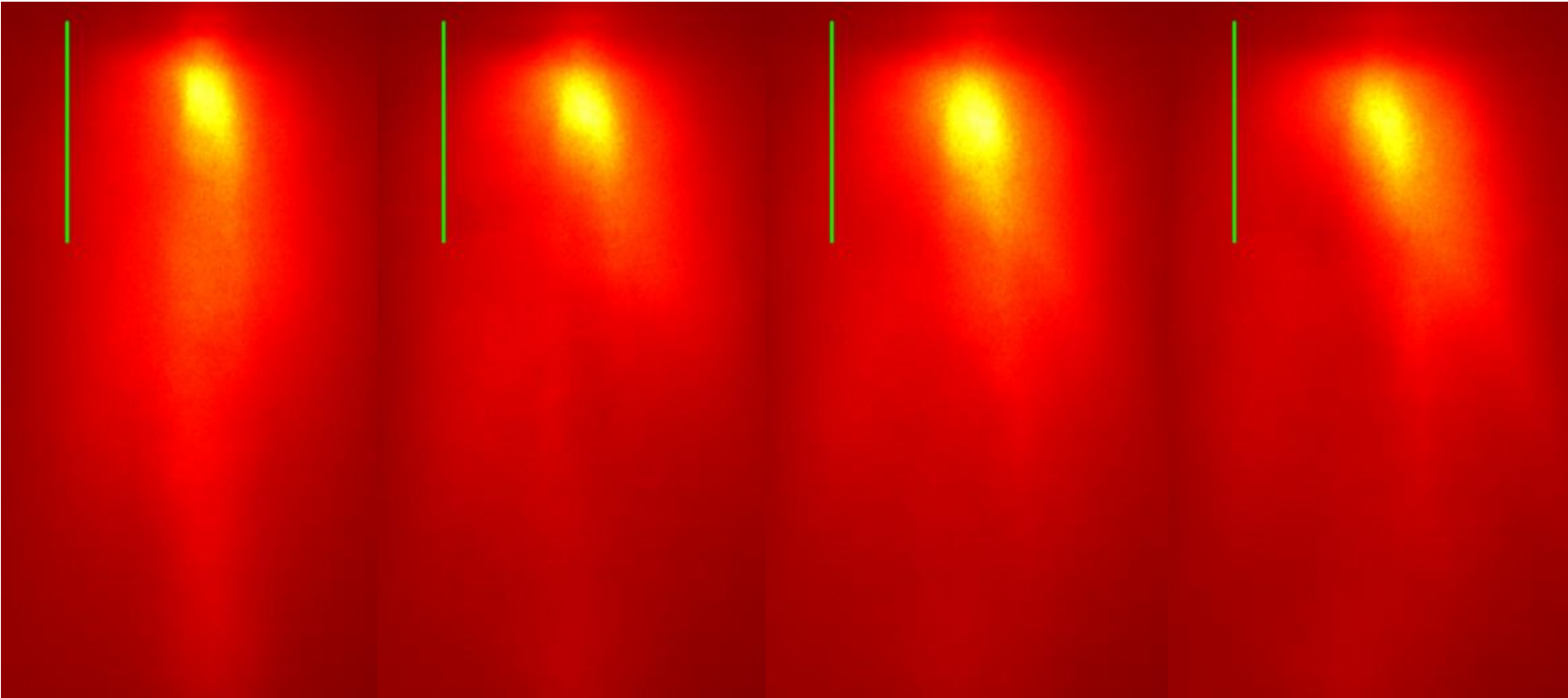
- **From the OH* there is an asymmetry depending on *J*.**

Asymmetric Cone Angle
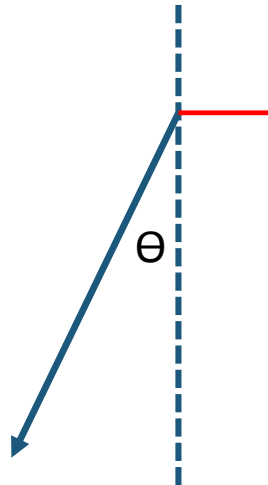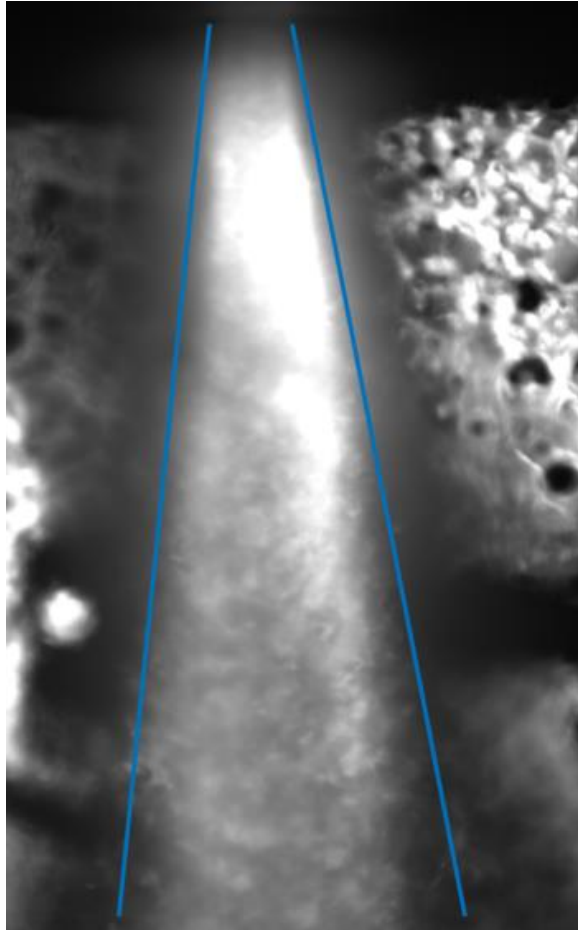
J	Left Ɵ °	Right Ɵ °
4.4	5.27	10.45
4.8	5.79	9.94
5.5	6.84	9.90
6.5	5.58	7.88

- **The asymmetry is also present in the cone angle.**

Proper Orthogonal Decomposition

In POD the flow field is decomposed into uncorrelated coherent structures with it corresponds energy content and temporal evolution.

- Perform proper orthogonal decomposition (POD) on fluctuating component of the J= 4.8 condition.

- POD was used to study the large scale structures associated with the reacting flow. Particularly the soot cloud and its rotation about the central oxygen core.

- POD was applied for the three optical methods.

- Performed POD on the data collected at 1000 Hz over one second.

$$I(x, y, t) = U\Sigma V'$$

data analysis as a matrix decomposition

Peter Schmid, 2013
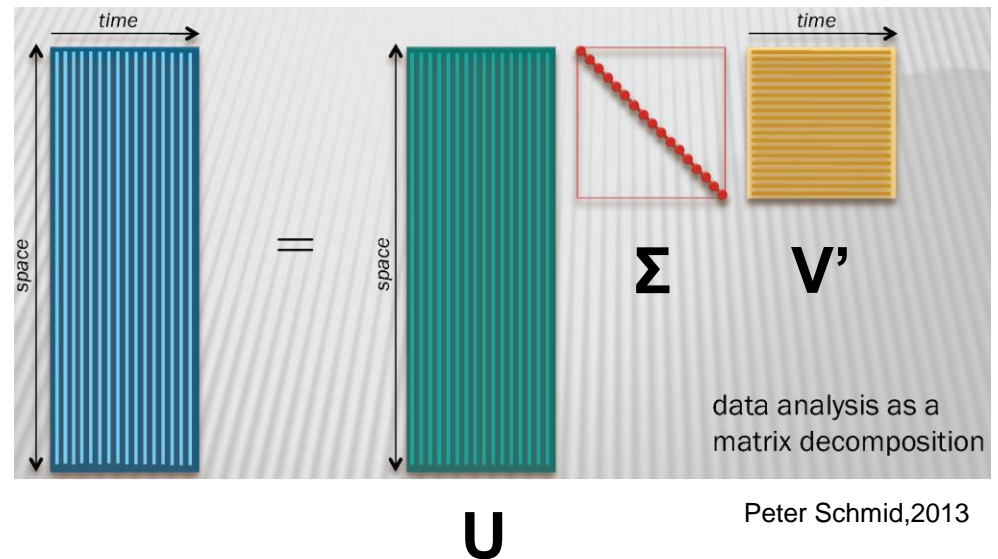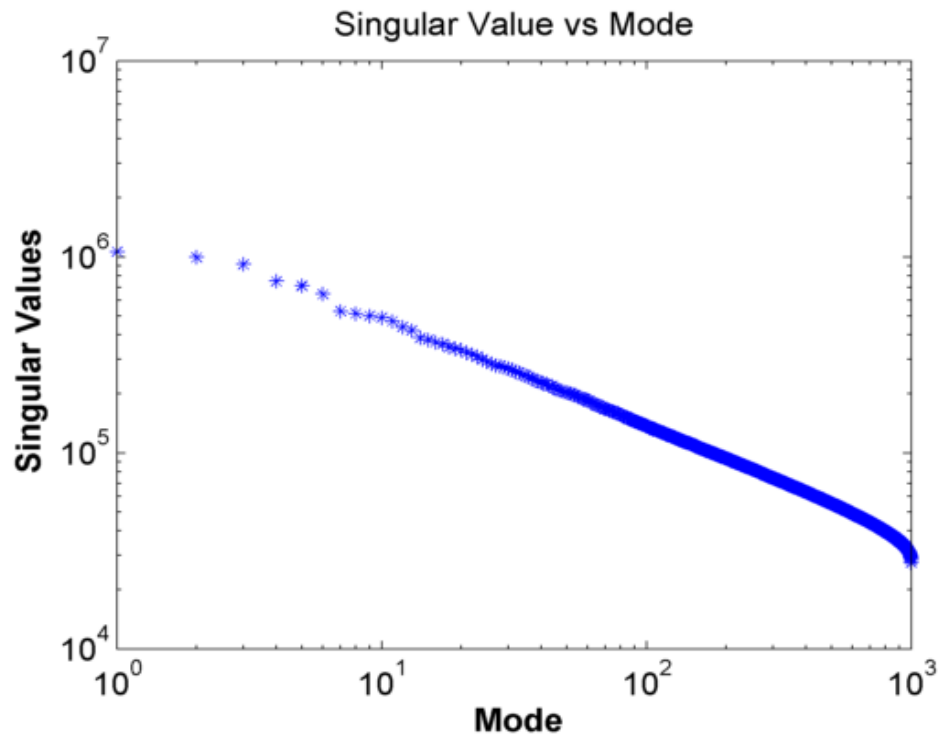
Shadowgraph

CH*
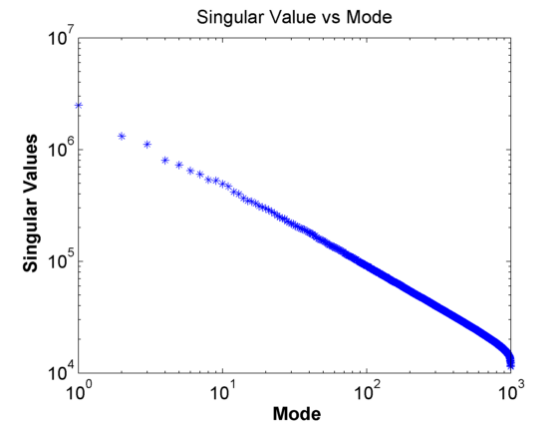
OH*
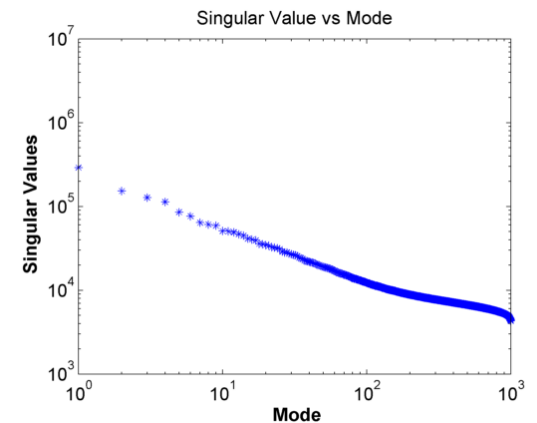
- **No dominant modes are present**

POD Eigen-Modes

CH*

OH*

Shadowgraph

- **No dominant modes are present**

OH*
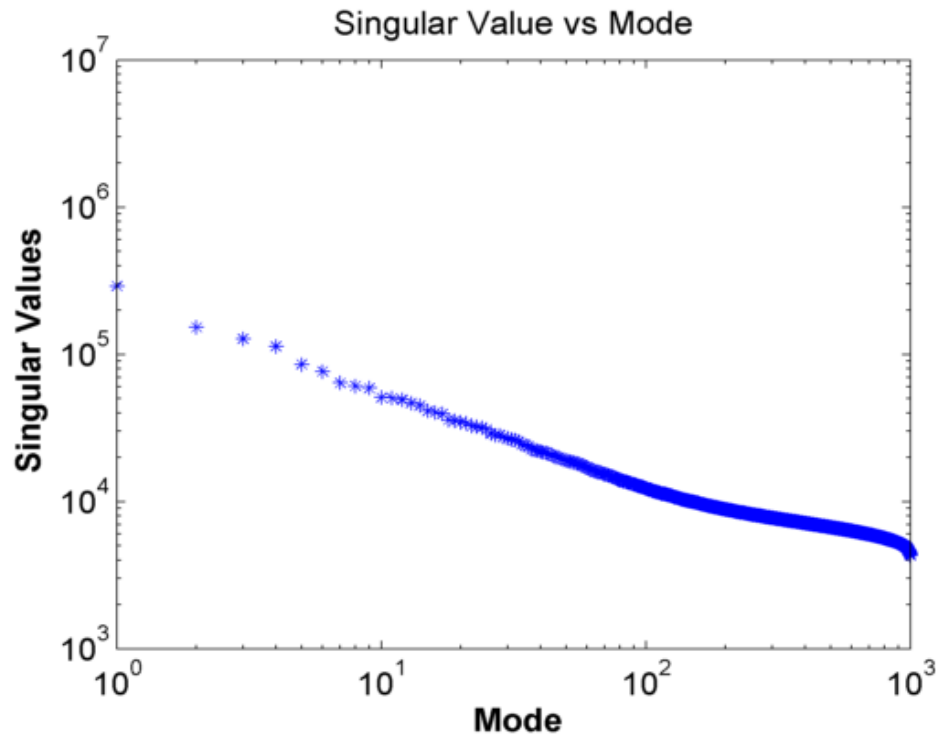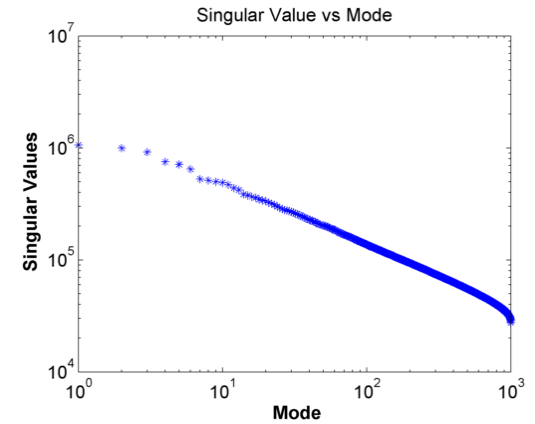
Shadowgraph

CH*
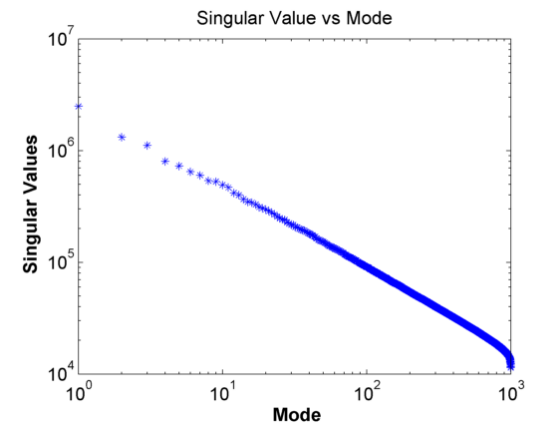
- **No dominant modes are present**
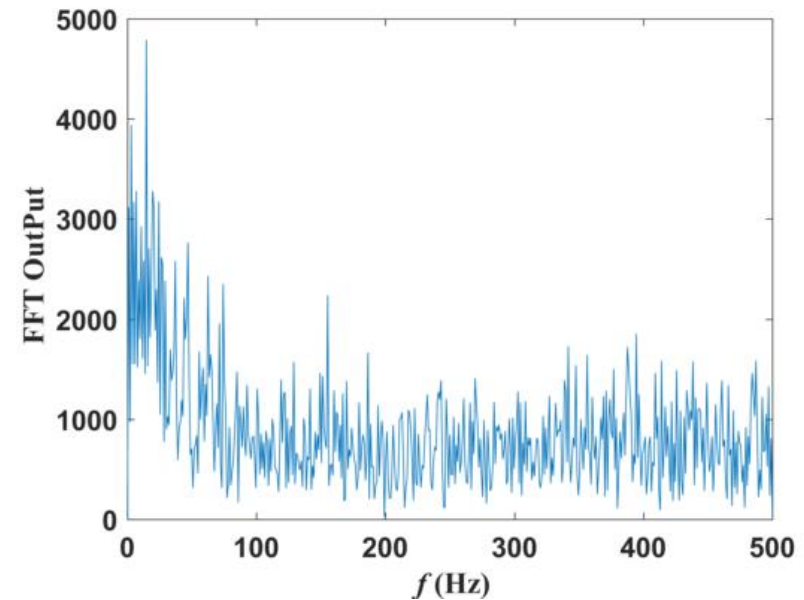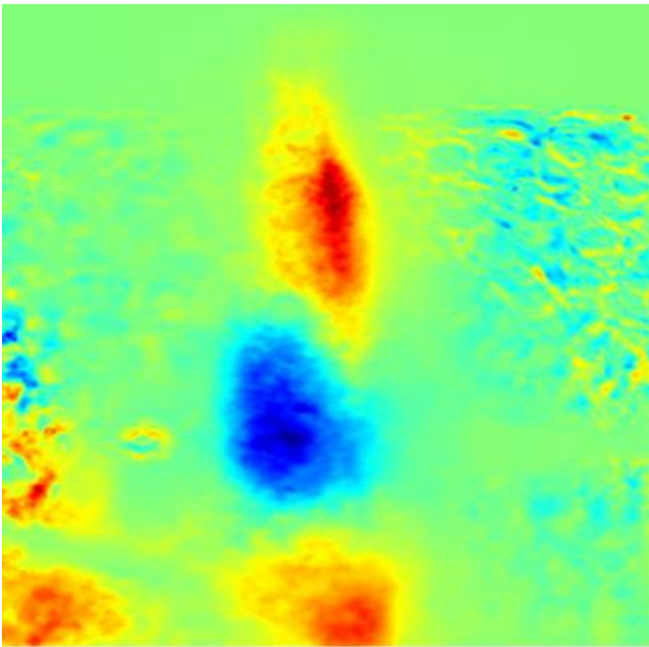
Shadowgraph

- **Pattern represents the soot cloud rotation about the oxygen core.**

Forced Results (J = 4.8)

Shadowgraph (25 kHz)
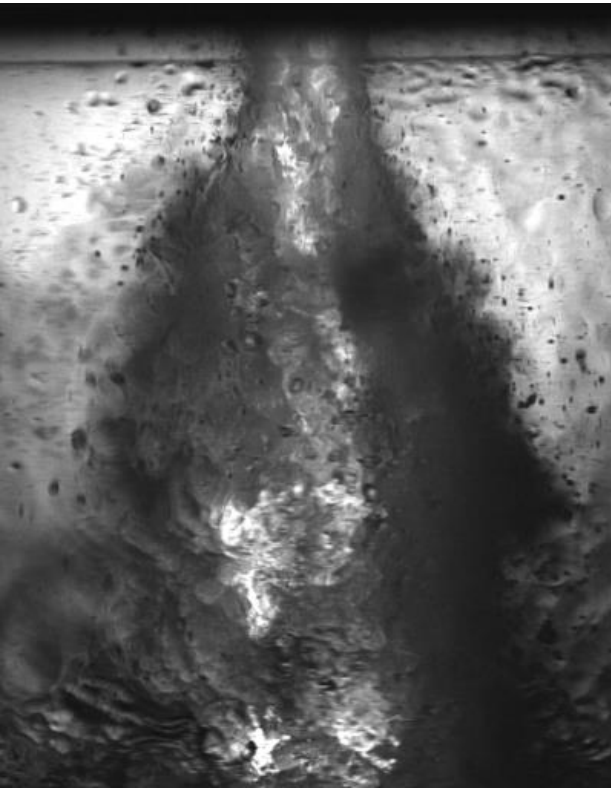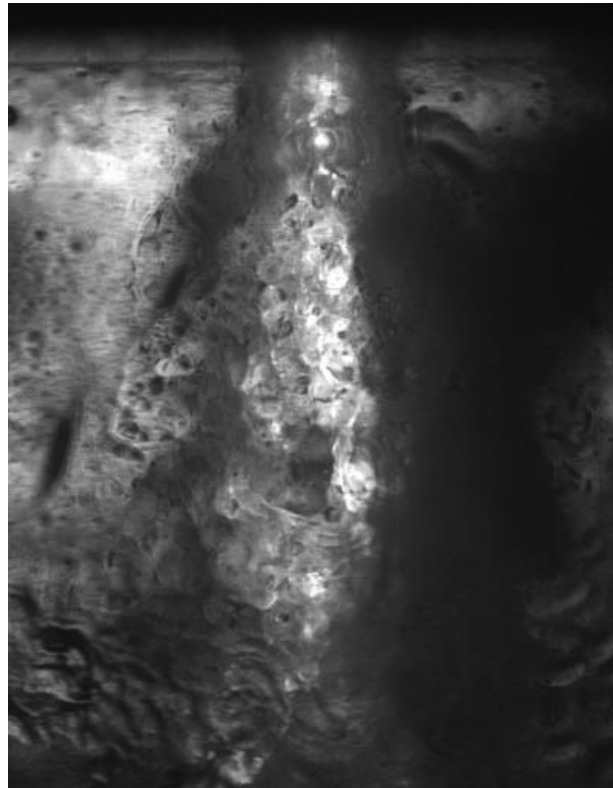
Unforced   1920 HZ   3060 HZ
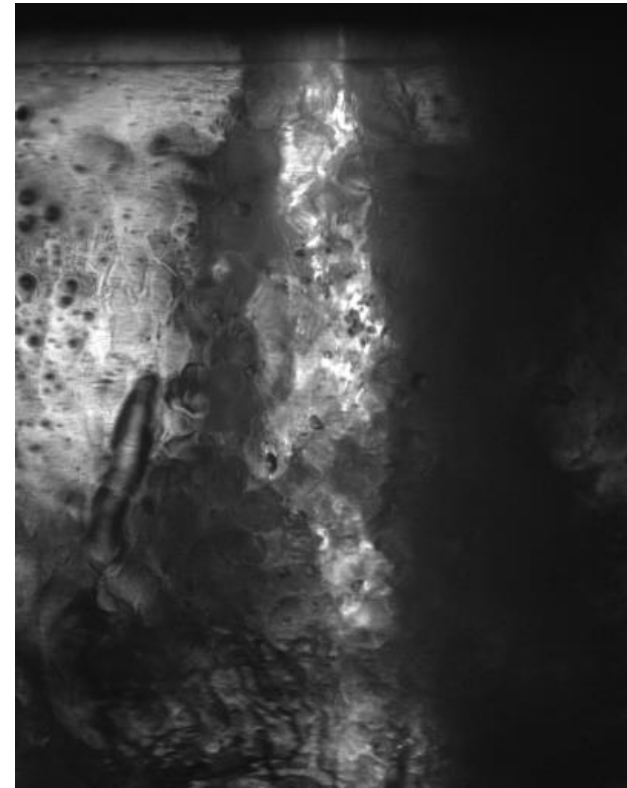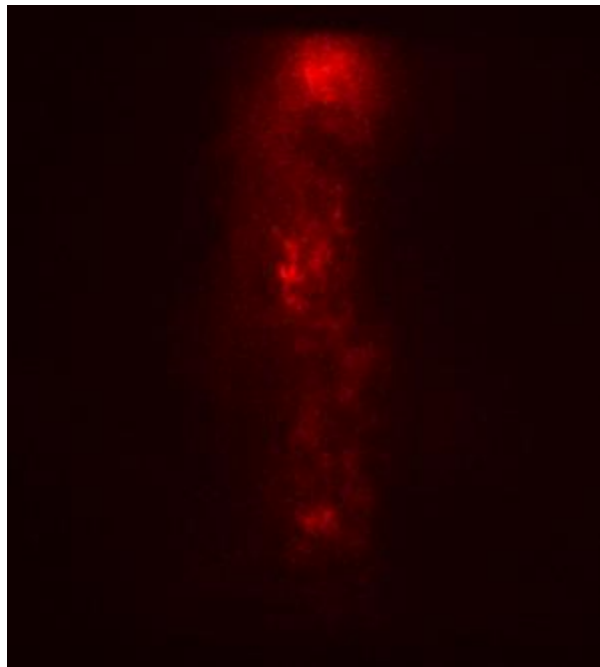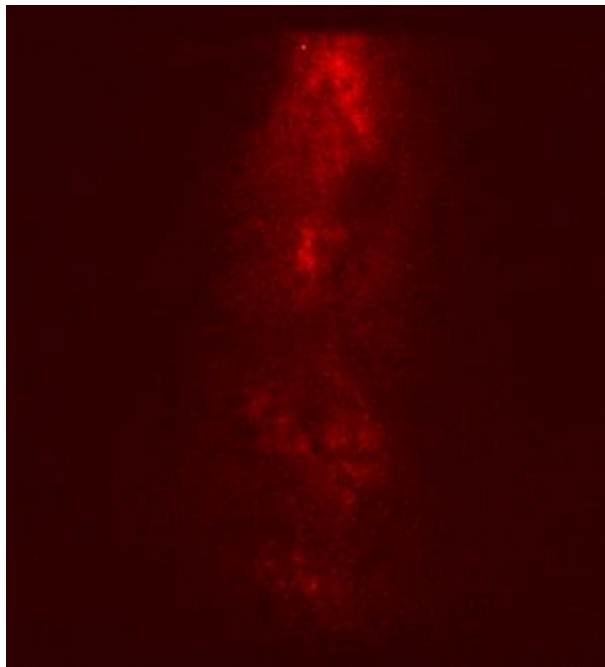
Forced Results (J= 4.8)

CH* (25 kHz)

Unforced

1920 HZ

3060 HZ
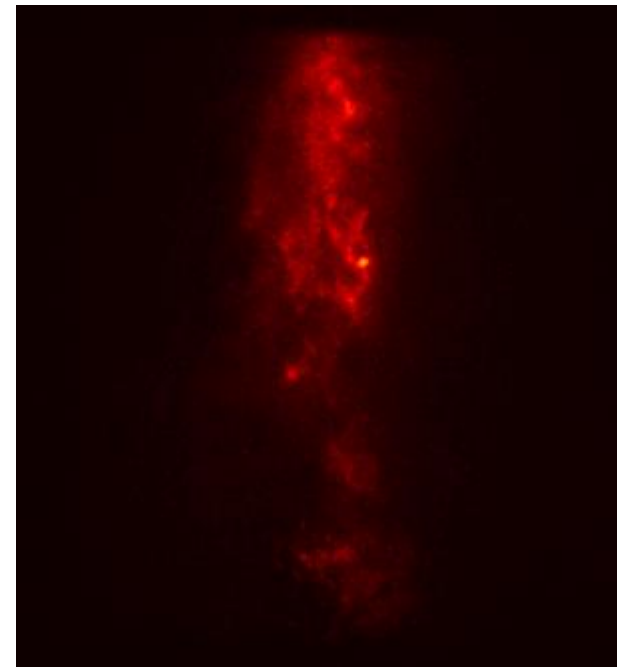
Dynamic Mode Decomposition

Extract spectrally-pure temporal modes with detailed spatial mode shapes
- Schmid (2010) and Rowley et al. (2009)
- Employ time-averaged amplitude measurement described by Alenius (2014)
- 2000 samples used

Amplitude of mode at t = 0

$$I(x, y, t) = \mathrm{Re}\left(\sum_{i=1}^{n} \widetilde{A}_i \exp(\widetilde{\lambda}_i t) \widetilde{D}_i(x, y) \right)$$

Accounts for growth of mode in time as well as temporal frequency

Complex spatial mode shape

Properties of DMD
- Isolates response of flow at forcing frequency and harmonics
- Single modes can reconstruct convective processes (POD requires two modes)
- Less efficient at reconstructing signal energy compared to POD
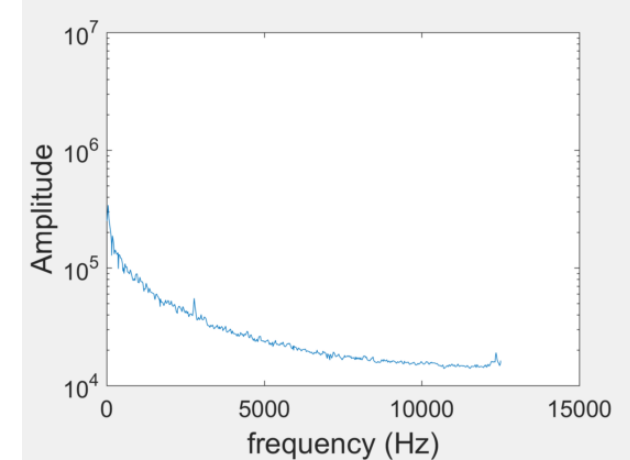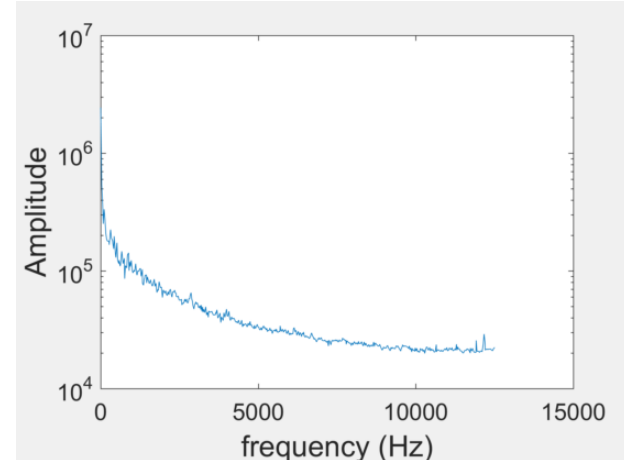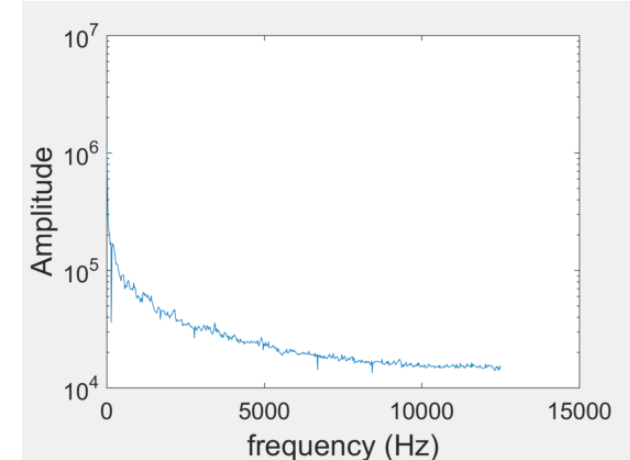
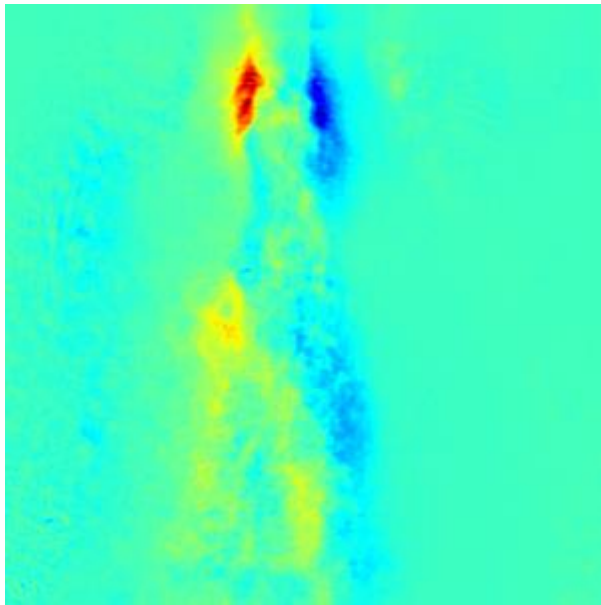# Dynamic Mode Decomposition Shadowgraph
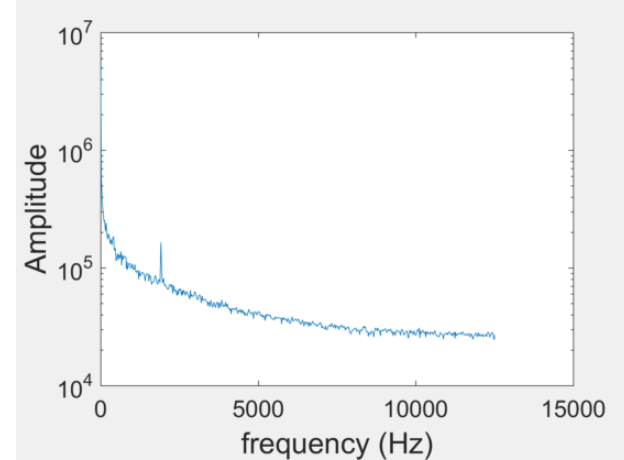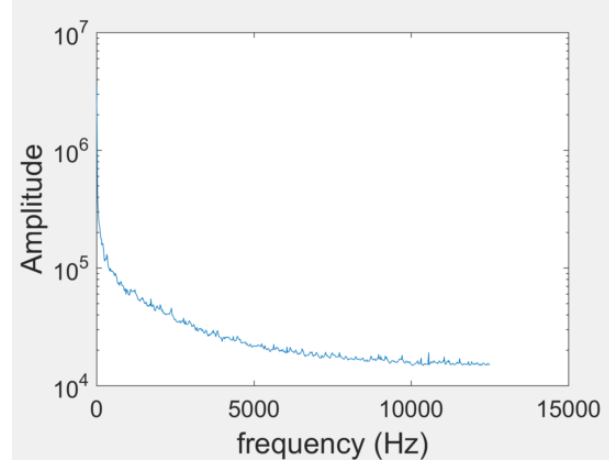
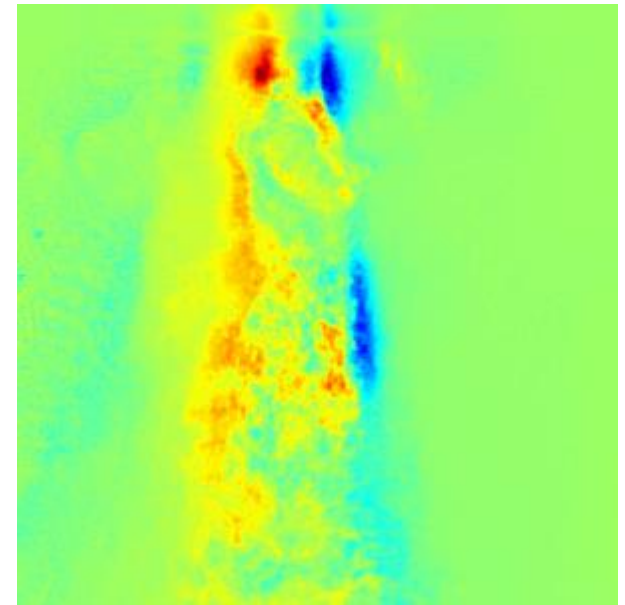- **The flow was receptive to 1920 Hz and 3060 Hz forcing.**

DMD Results

1920 Hz

3060 Hz

- **The dominant DMD spatial physically represents in-plane flapping of the oxygen core.**

Conclusion

- **Flame appears to be attached at the nozzle exit from the shadowgraph images.**

- **Soot clouds block optical view to the flame anchoring regions in the CH* and OH* images**

- **Soot clouds are created at the periphery of the liquid film and rotate around the gaseous oxygen core.**

- **The POD analysis, the soot clouds are large flow structure associated with the flow and are highly stochastic.**

- **The injector has selective forcing frequencies to which it is most receptive.**
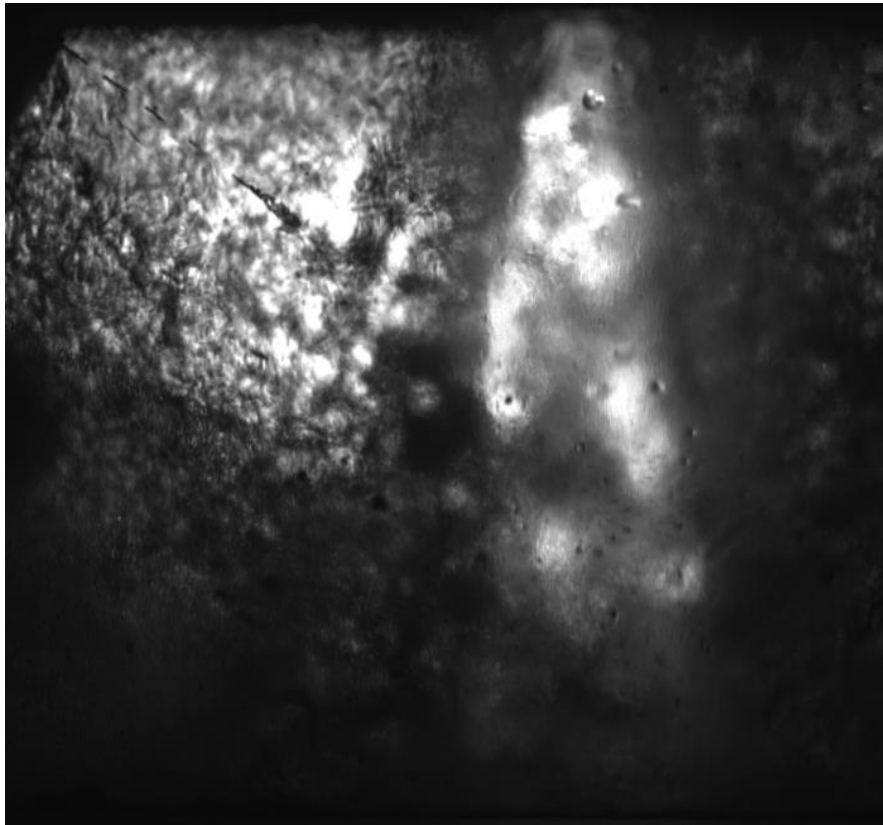
- **The DMD analysis detects the in-plane flapping motion of the oxygen core.**

Window Coating

No coating

Window Coated